

Protocol Discovery for the Quantum Control of Majoranas by Differential Programming and Natural Evolution Strategies

Luuk Coopmans,^{1,2,*} Di Luo,^{3,*} Graham Kells,¹ Bryan K. Clark,³ and Juan Carrasquilla^{4,5}

¹*Dublin Institute for Advanced Studies, School of Theoretical Physics, 10 Burlington Rd, Dublin, Ireland.*

²*School of Physics, Trinity College Dublin, College Green, Dublin 2, Ireland*

³*Department of Physics and IQIIST and Institute for Condensed Matter Theory, University of Illinois at Urbana-Champaign, IL 61801, USA*

⁴*Vector Institute for Artificial Intelligence, MaRS Centre, Toronto, Ontario, Canada*

⁵*Department of Physics and Astronomy, University of Waterloo, Ontario, N2L 3G1, Canada*

(Dated: July 5, 2022)

Quantum control, which refers to the active manipulation of physical systems described by the laws of quantum mechanics, constitutes an essential ingredient for the development of quantum technology. Here we apply Differentiable Programming (DP) and Natural Evolution Strategies (NES) to the optimal transport of Majorana zero modes in large superconducting nano-wires, a key element to the success of Majorana-based topological quantum computation. We formulate the motion control of Majorana fermions as an optimization problem for which we propose a new categorization of four different regimes with respect to the critical velocity of the system and the total transport time. In addition to correctly recovering the anticipated smooth protocols in the adiabatic regime, our algorithms uncover efficient but strikingly counter-intuitive motion strategies in the non-adiabatic regime. The emergent picture reveals a simple but high fidelity strategy that makes use of pulse-like jumps at the beginning and the end of the protocol with a period of constant velocity in between the jumps, which we dub the jump-move-jump protocol. We provide a transparent semi-analytical picture, which uses the sudden approximation and a reformulation of the Majorana motion in a moving frame, to illuminate the key characteristics of the jump-move-jump control strategy. Our results demonstrate that machine learning for quantum control can be applied efficiently to quantum many-body dynamical systems with performance levels that make it relevant to the realization of large-scale quantum technology.

I. INTRODUCTION

Through the use of a wide array of promising experimental platforms ranging from superconducting qubits [1] to trapped ions [2–4], optical lattices [5] and nitrogen-vacancy centers [6, 7], scientists are exploring groundbreaking ways to build quantum technology with an eye on deepening our understanding of complex natural systems, improving artificial intelligence, and impacting industry more broadly. While promising, several fundamental and practical difficulties must be overcome for quantum machines to become practical [8]. Quantum control, which studies the manipulation of physical systems whose behaviour is dominated by the laws of quantum mechanics, remains a fundamental ingredient in the quest for practical quantum technology. Thus, the development of principles and strategies for quantum control [9–13] remains an essential task for future quantum technologies [14], e.g., in the preparation of complex quantum states in quantum computing and quantum simulators.

The practical encoding and manipulation of quantum information has however been hampered by the presence of noise and decoherence inherent to brittle quantum devices. Majorana zero modes, which are special zero-energy quasi-particles with non-abelian braiding statistics that can be realized in proximity-coupled supercon-

ductors [15–24], represent a promising alternative approach due to their non-local nature and anticipated topological protection against local errors [25–30]. The key to manipulating this topologically encoded quantum information is the development of protocols to transport the Majoranas, as will be necessary for their braiding and measurement. While the simplest approaches propose to move the Majoranas adiabatically, decoherence processes such as quasiparticle poisoning [31], motivate the need for faster and more efficient control protocols.

In this context, machine learning (ML) offers a powerful and unifying approach to the study, design, benchmarking, and control of quantum systems and devices. Motivated by a series of remarkable technological breakthroughs in research areas as diverse as computer vision [32], natural language processing [33] and genomics [34], physicists have started to explore the potential of ML for fundamental research [35]. In particular, researchers interested in quantum many-body physics have initiated the development of a machine learning perspective on the many-body problem [36] with recent advances such as neural network representation of quantum states [37–48], neural network tomography [49–51], machine learning classification of phases [38], as well as advances in quantum chemistry [52–54], density functional theory [55, 56] and the acceleration of Monte Carlo simulations [57–59] among many others [36, 60]. ML applications in the context of quantum control [61–63] are largely based on reinforcement learning (RL) techniques,

* Co-first authors.

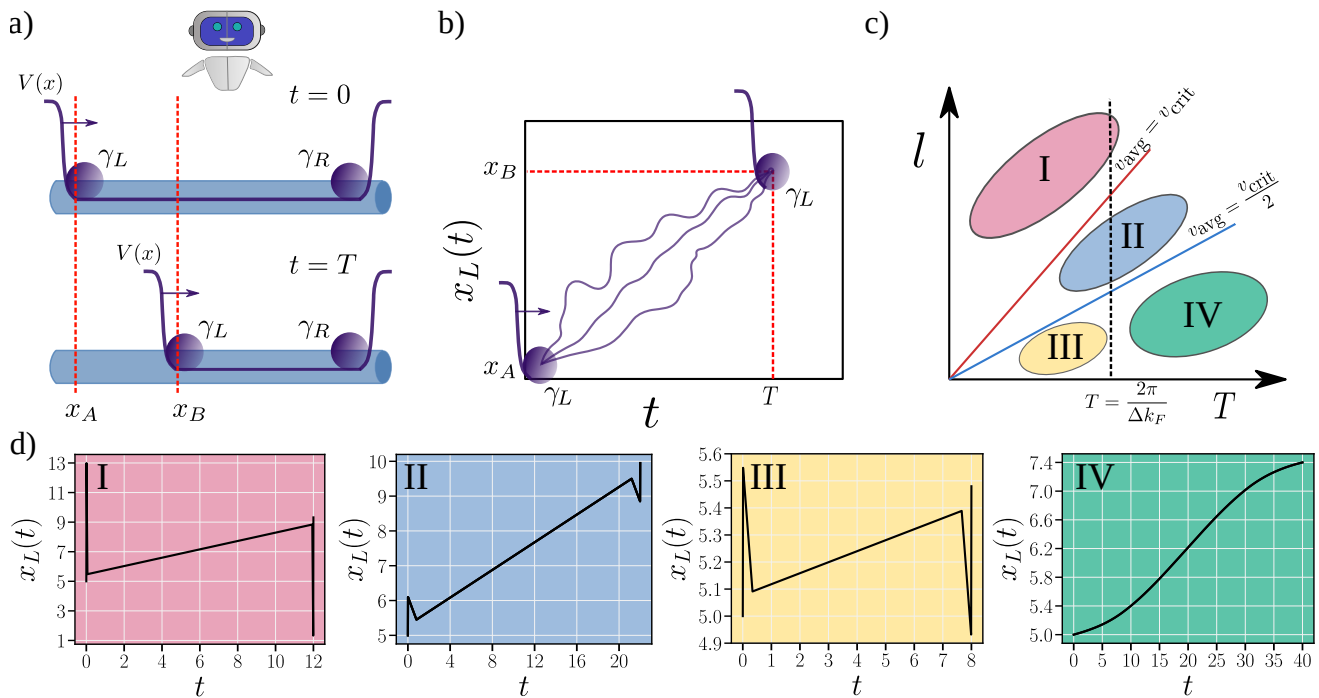


FIG. 1. a) In the Majorana Game the agent moves the left Majorana γ_L from a position x_A to a position x_B by tuning the external potential profile $V(x, t)$. b) The agent attempts different movement paths and tries to find the optimal one that minimizes the infidelity $\mathcal{I}(T)$. c) Different Majorana control regimes and their corresponding strategies (boxes in d)): I) Critical regime ($v_{\text{avg}} > v_{\text{crit}}$), II) sub-critical regime ($v_{\text{crit}}/2 < v_{\text{avg}} < v_{\text{crit}}$), III) short time T , low velocity regime and IV) (super)-adiabatic regime (long time T and low velocity v_{avg}). d) In regimes I-II-III we find the jump-move-jump (JMJ) strategy whereas in regime IV we recover a smooth super-adiabatic protocol. The infidelities are $\mathcal{I}(T) = 0.3575$ in regime I, $\mathcal{I}(T) = 0.1589$ in II, $\mathcal{I}(T) = 0.0057$ in III and $\mathcal{I}(T) = 0.0005$ in regime IV; the parameters for the JMJ strategies displayed in regimes I, II, III can be found in App. E and we have set $x_L(0) = x_A = 5.0$ to ensure a smooth potential profile $V(x, t)$.

which are the key ingredient behind major artificial intelligence breakthroughs in game play [64, 65]. A RL perspective on quantum control has been developed in the context of quantum state preparation [61], where the authors reexamine the quantum state preparation in terms of a modified version of the Watkins Q-learning algorithm [66]. Likewise, Ref. [62] considers the problem of gate synthesis from a RL viewpoint.

In this work we exploit Differential Programming (DP) [67] and Natural Evolutionary Strategies (NES) [68] to find optimal strategies to transport Majorana zero modes. We reformulate the complex task of transporting a Majorana zero mode as a quantum control optimization problem amenable to advanced ML techniques. This can be most easily understood from a reinforcement learning perspective where the movement of the Majoranas can be recast as a “game”, see Fig. 1. In this game the player (agent) has to move a Majorana from a position x_A to a position x_B in a fixed amount of time T . At the end of the game the agent gets rewarded depending on how well the Majorana reached its target state at position x_B . The objective of the agent is to learn the best strategy (path of the Majorana) that maximizes the reward.

Our machine learning techniques discover a novel and counter-intuitive approach to transporting Majorana

zero modes, here dubbed the *jump-move-jump* approach and exemplified in Fig. 1, which yields a high fidelity control significantly superior in terms of speed and quality to previous strategies applied to this problem [69–71]. The jump-move-jump protocol, which is relevant for transporting Majoranas over a large distance l in a short time T , makes use of pulse-like jumps at the beginning and end of the protocol (see regions I-III of Fig. 1), with a period of nearly constant velocity between the jumps. This is particularly interesting given the previous results for simpler models showed that bang-bang protocols [70] were the most efficient approach to this form of quantum control.

Using the insight gleaned from our ML-inspired control protocols, we construct the core strategy for these paths and provide a theoretical understanding for the protocol by analyzing the motion of the Majoranas in a moving frame. We find that these protocols simultaneously use the stability of the system at finite velocities together with the fact that small sudden jumps in wall position do not significantly reduce the ground-state fidelity. In contrast, in the limit where there is a significant total time T to move a relatively small distance l , the best approach is to follow smooth protocols that follow an adiabatic path. Our ML technology recovers these pro-

protocols without any prior knowledge (see region IV of Fig. 1).

II. SETUP OF THE MAJORANA CONTROL PROBLEM

To model the movement of the Majorana zero modes in superconducting nano-wires we use a one-dimensional (1D) Kitaev Chain [25] described by the Hamiltonian

$$\mathcal{H}(t) = - \sum_{x=1}^N [\mu(x) - V(x, t)] (c_x^\dagger c_x - 1/2) - w \sum_{x=1}^{N-1} (c_x^\dagger c_{x+1} + h.c.) + \Delta \sum_{x=1}^{N-1} (c_x^\dagger c_{x+1}^\dagger + h.c.), \quad (1)$$

where $c_x^{(\dagger)}$ are fermionic annihilation (creation) operators, $\mu(x)$ the onsite chemical potential, $V(x, t)$ a time-dependent external potential, w the hopping amplitude and Δ the p-wave superconducting gap. This model can be realized effectively in variety of setups by proximity coupling to a conventional s-wave superconductor [15–17, 19, 20, 72–74]. When $|\mu| \geq |2w|$ the gap in the energy spectrum closes inducing a transition to a topological trivial phase [25, 75]. For an open chain, a pair of Majorana zero-modes are found to reside on the edges of the wire if the bulk is topologically non-trivial. The existence of such Majorana modes implies the existence of a degenerate space of ground states. The ground state of the system is protected by a robust topological energy gap, which in the continuum limit of the model is given by $\min[\mu_c, \Delta_c k_F]$. As a consequence of this protection, two pairs of Majorana zero-modes can be used to produce a qubit whose information content is protected non-locally [27].

Manipulation of the information encoded in the ground state requires the braiding of the Majorana quasiparticles [18, 26, 28, 29, 76–79], while staying as much as possible within the degenerate ground-state space. To achieve this, a generic strategy is to try to perform the braiding adiabatically. An adiabatic path generically must have a total time T larger than the inverse gap; in practice the size of the topological gap makes such a strategy prohibitively slow in view of numerous sources of decoherence in proximity coupled setups [31, 80–85].

One possible strategy here is to shortcut the adiabatic constraint [86]. In practice however the application of shortcuts to adiabaticity in this setup (see e.g. [87]) requires precise control of the couplings between neighbouring Majoranas, a level of precision that is beyond current experimental devices. Another strategy here however is to examine protocols that operate with a cruder level of control [69, 71, 88]. To this end, and to have smooth control over the position of the Majorana bound states on the lattice, we encode the external potential profile as

$$V(x, t) = V_{\text{height}} [f(x - x_L(t)) + f(x_R - x)] \quad (2)$$

where V_{height} is the maximum height of the outer potential walls and $f(x) = 1/(1 + \exp(x/\sigma))$ is a sigmoid function shifted by the wall positions $x_{L(R)}$ (Fig. 1 a). The Majoranas are localized at the outer edges of the potential profile, which can be seen as domain walls between topological and non-topological phases since $V_{\text{height}} \gg 2w$. The position of these domain walls can be controlled through $x_{L(R)}$; to move the left Majorana we give the agent control over $x_L(t)$ as a function of time.

The motivation for this specific form of potential profile comes from experimental proposals for moving the Majorana by the so called piano-key potentials [18, 69, 89]. In this proposal the position of the domain wall in the wire is controlled by applying gate electrodes. At variance with protocols found in [70], the presence of nonlinearities in the potential profile implies that bang-bang protocols, which are expected for linear control [90, 91], may no longer be optimal. As a consequence of this, it is conceivable that the space of possible solutions is expanded in our setting.

The Majorana game starts at $t = 0$ with the system in the groundstate of Eq. 1 with $x_L(0) = x_A$. The aim is to reach the groundstate $|\Psi_B\rangle$ with $x_L(T) = x_B$ located at a distance $x_B - x_A = l$ spending a total time T . A natural choice to quantify the accuracy of the protocol is the infidelity

$$\mathcal{I}(T) = 1 - |\langle \psi_B | e^{-i \int_0^T \mathcal{H}(t) dt} | \psi_A \rangle|^2 \equiv 1 - \mathcal{F}(T). \quad (3)$$

Here, $\mathcal{H}(t)$ is the time-dependent Hamiltonian that describes the Majorana wire setup Eq. 1 during the protocol. Whereas $\mathcal{I}(T) = 0$ means that we have fully preserved the encoded quantum information, $\mathcal{I}(T) = 1$ implies that information has been completely lost.

A key timescale related to the control problem is $T_{\text{res}} = \frac{2\pi}{\Delta k_F}$, which naturally arises from the response of the system to boundary wall oscillations (see [71] and App. A). T_{res} corresponds to the time above which one can make changes slowly enough for genuinely super-adiabatic motion [69, 92, 93]. Super-adiabaticity in this scenario allows the static ground state to be accelerated into the ground state of a moving frame, provided the transition is done slowly enough, i.e., in times large compared to T_{res} . However another important additional physical constraint here is the presence of a critical velocity $v_{\text{crit}} = \Delta$ [69, 88] above which the moving frame Hamiltonian becomes gapless (App. A) and the ground states lose their topological protection.

Based on this we divide up the Majorana control problem into four different regimes (I-IV) (see Fig. 1 c). Region I corresponds to the critical regime in which the Majorana must move on average $v_{\text{avg}} = l/T$ above the critical velocity. In this regime the ground state fidelity is expected to rapidly decrease to zero. Regime II is the sub-critical regime for which the velocity is on average close to but nonetheless below v_{crit} . Regime III is defined for the times that are short with respect to the resonance time T_{res} but also has low velocity. Finally regime IV is the adiabatic regime in which we are far above T_{res} and

we expect super-adiabatic protocols [69, 71] from earlier studies to be optimal.

III. MACHINE LEARNING METHODS

In our study we apply two machine learning strategies, namely Differential Programming (DP) and Natural Evolution Strategies (NES), to minimize the infidelity Eq. 3 with respect to the position of the domain wall $x_L(t)$.¹ In this section we briefly discuss these methods in a way that directly applies to our Majorana control setup. For the interested reader we provide the corresponding programming codes in [94].

A. Differential Programming

DP is a programming paradigm to evaluate gradients of computer programs [95] that has been recently introduced as an optimization method in physics applications like Tensor Networks [96, 97], Monte Carlo [40, 98, 99], optimal control [63, 100]. DP obtains numerically exact gradients with similar computational complexity as the forward evaluation of the computer program due to the use of backward propagation [101].

In our Majorana control optimization problem we are interested in the total derivative of the infidelity with respect to the control $\frac{d\mathcal{I}(T)}{dx_L(t)}$. As shown in App. B, the algorithm to compute $\mathcal{I}(T)$ consists of a sequence of elementary operations f_i , in DP language known as primitives, which maps the input control $x_L(t)$ to the value of the infidelity by $\mathcal{I}(T) = f_n \circ f_{n-1} \circ \dots \circ f_1(x_L(t))$. Moreover, the derivatives of each individual operation f_i are known and the total derivative $\frac{d\mathcal{I}(T)}{dx_L(t)}$ can be assembled by recursively applying the chain rule with automatic differentiation (see App. B).

In practice, we write a code to evaluate the real-time dynamics of the Majorana induced by the time-dependent profile $V(x, t)$ such that all the individual operations are differentiable. To obtain the necessary gradients we use a language that supports automatic differentiation, which in our case is the JAX library [102]. The gradients are used to minimize the infidelity of the final state through gradient descent. This is done iteratively, where at each iteration of the algorithm the protocol is updated as $x_L(t) \rightarrow x_L(t) - \nabla_{x_L(t)} \mathcal{I}(T)$. Moreover since neural networks consist of differentiable elementary operations, we also explore representing and training the control $x_L(t)$ as the output of a neural network.

B. Natural Evolution Strategies

Evolution Strategies is a family of black-box optimization algorithms inspired by natural evolution [68, 103]. These methodologies have been recently revisited in the context of machine learning [104], in particular in reinforcement learning [105], where OpenAI demonstrated that a particular incarnation of the algorithm called natural evolution strategies (NES) offers a powerful alternative to popular Markov-decision process-based reinforcement learning methods [106]. NES starts with an objective function $F(\phi)$ that acts on parameters ϕ from a population described by a distribution p_θ , where θ parameterizes the population distribution. In our work, we choose the objective function $F(\phi)$ to be the infidelity $\mathcal{I}(T, \phi)$ in Eq. 3. Depending on the setting, the parameter ϕ corresponds to either the position profile $x_L(t)$, the velocity $v_L(t) = \dot{x}_L(t)$ or the parameters of a neural network whose output is $x_L(t) = \text{NN}_\phi(t)$.

The NES algorithm proceeds to optimize the expectation value of the objective function $\mathbb{E}_{\phi \sim p_\theta} [\mathcal{I}(T, \phi)]$ over the population. We choose p_θ to be Gaussian distribution with mean θ and diagonal covariance matrix $\Sigma = \sigma^2 I$ with $\sigma = 0.1$, i.e., $\mathcal{N}(\theta, \sigma^2 I)$. It follows that the gradient of the cost function is (see App. C)

$$\begin{aligned} \nabla_\theta \mathbb{E}_{\phi \sim \mathcal{N}(\theta, \sigma^2 I)} [\mathcal{I}(T, \phi)] &= \nabla_\theta \mathbb{E}_{\epsilon \sim \mathcal{N}(0, I)} [\mathcal{I}(T, \theta + \sigma \epsilon)] \\ &= \mathbb{E}_{\epsilon \sim \mathcal{N}(0, I)} [\mathcal{I}(T, \theta + \sigma \epsilon) \epsilon / \sigma]. \end{aligned} \quad (4)$$

This equation provides an efficient way for computing gradients without differentiation, but instead through the expectation of the objective function. Notice that $\mathbb{E}_{\epsilon \sim \mathcal{N}(0, I)} [\mathcal{I}(T, \theta) \epsilon / \sigma] = 0$, which implies the above equation is equivalent to $\mathbb{E}_{\epsilon \sim \mathcal{N}(0, I)} [(I(T, \theta + \sigma \epsilon) - I(T, \theta)) \epsilon / \sigma]$. This means that the estimation of the gradient can be seen as the finite difference of the objective function with random search [105]. To update the parameters θ , we apply gradient descent to θ with Eq. 4.

IV. MACHINE LEARNED STRATEGIES FOR MAJORANA CONTROL

Our main objective is to investigate the use of DP and NES for the motion of the Majorana modes in the four different movement regimes I-IV. We choose four different points (l, T) (which fixes $v_{\text{avg}} = l/T$) each of which belongs to a different regime. For each of these points we apply the optimization algorithms to minimize the infidelity $\mathcal{I}(T)$ in Eq. 3 with respect to the control of the domain wall. The control can be parameterized by either the wall position $x_L(t)$, the wall velocity $v_L(t)$ or a neural network $x_L(t) = \text{NN}_\theta(t)$, where θ represent the parameters in the neural network. We tested all these different parameterizations (see App. D) and in the following we focus on the parameterization choices that give the best performance (the lowest infidelity values).

¹ We note that the control can also be represented by the velocity or a neural network parameterization of the domain wall from which the position $x_L(t)$ can be extracted.

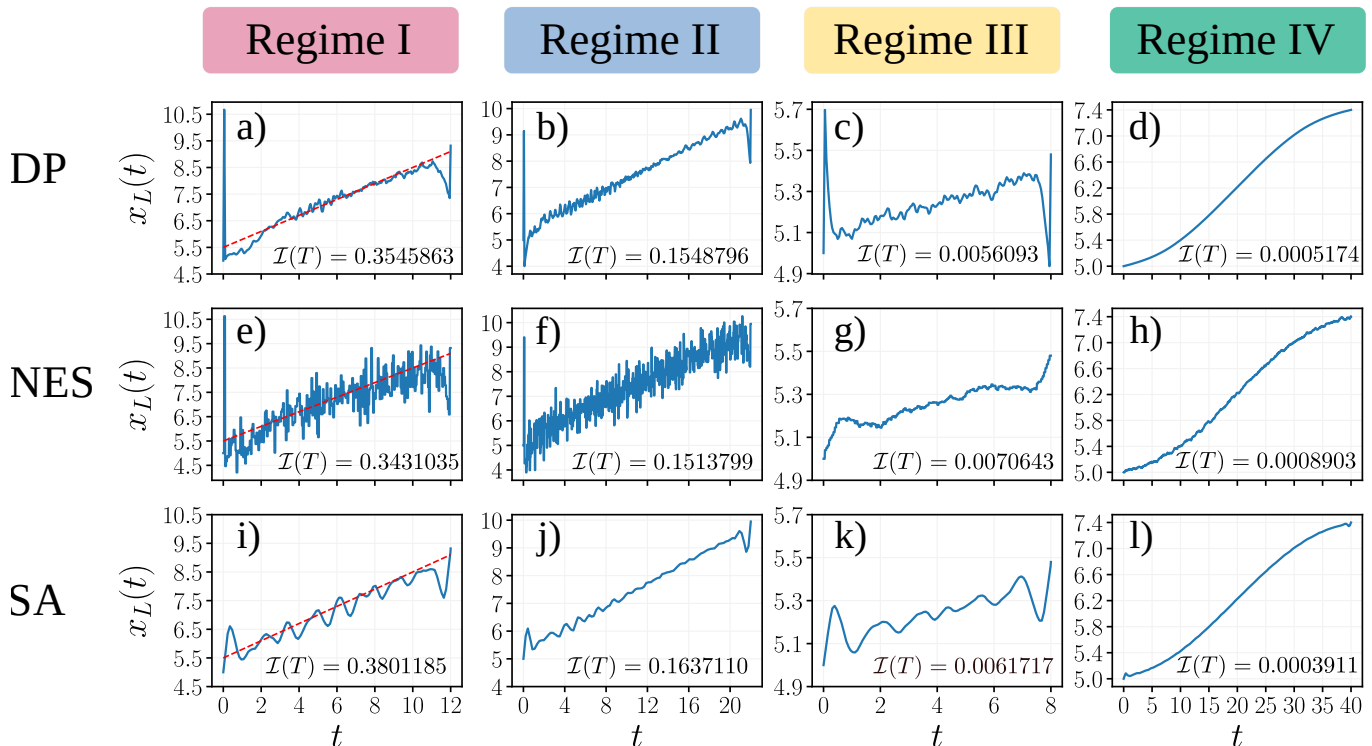


FIG. 2. Overview of the optimal controls in the four different Majorana motion regimes (I-IV) obtained after optimization with Differential Programming (DP), Natural Evolutionary Strategies (NES) and Simulated Annealing (SA). In all panels we plot the domain wall position $x_L(t)$ as a function of time starting from $x_L(0) = x_A = 5.0$. The red dotted line in regime I has a slope equal to the critical velocity. Regimes I-III show a pulse like motion at the edges and an on average constant velocity in the bulk of the protocol. In regime IV the strategy is to slowly build up to constant speed and then slow down again. In these simulations we set $N = 110$, $\mu = 1$, $w = 1$, $\Delta = 0.3$, $V_{\text{height}} = 30.1$, and $\sigma = 1$. The constraint parameters (l, T) are given by $\{(4.32, 12), (4.95, 22), (0.48, 8), (2.4, 40)\}$ for regimes I,II,III, and IV, respectively.

For the DP optimization, we first parameterize the wall position by a neural network $x_L(t) = \text{NN}_\theta(t)$ and use gradient descent to optimize it. We then take the resulting real-space profile $x_L(t)$ and directly re-optimize it in the position representation. We find that this two-step process is beneficial; while the initial NN stage allows a quick convergence to a smooth nearly-optimal control profile, the second step allows for additional fine-tuning and more abrupt changes in the protocol. The neural network $\text{NN}_\theta(t)$ used for these simulations consists of three layers of 100 neurons with Rectified Linear (Relu) activation functions followed by one output neuron with a sigmoid activation function. The parameters of this neural net are updated with a standard ADAM optimization algorithm [107] for which the learning rate is determined empirically. The NES optimization in regimes I/II is done with gradient descent directly on the wall position $x_L(t)$ and in regimes III/IV by running gradient descent on the wall velocity $v_L(t)$ from which the wall position can be extracted via integration $x_L(t) = x_A + \int_0^t v_L(t') dt'$.

The time-dependent simulations of the fermionic system are discretized over time with a small time resolution $dt = 0.01$. To ensure the algorithms are not exploiting the time discretization dt of the simulation, we allow the

ML algorithms control over only a coarse grained time scale $\Delta t \geq 10dt$. Moreover to probe the susceptibility of the optimized protocols to initial conditions, we repeat the optimizations a few times for several different starting configurations to ensure that the results are independent of the initialization.

The results for these optimizations in the four different regimes are shown in Fig. 2(a-h) and can be summarized as follows. In the regimes I-II-III we can identify clear similarities between all of the optimised strategies which display sudden movements (jumps) at the beginning and end, and more gradual rates of changes in the middle of the protocol.

The initial sudden movements can be roughly characterised by a rapid jump forward, followed by a less abrupt backward motion. The jumps near the end of the protocol display an analogous movements in the reverse order, although these are generally less pronounced.

The middle of the protocols consists of an approximately constant-velocity forward-motion that is dressed to various degrees with high frequency oscillations. We observe that the velocity in the middle part of the protocols is typically lower than v_{crit} even for regime I, where the total average velocity v_{avg} (including the sudden

movements) is above v_{crit} . The size and character of the additional oscillations largely depends on the optimization strategy being used.

The infidelity values we find in regimes I-II-III are significantly better compared to strategies like linear motion $x_L(t) = v_{\text{avg}}t$ or bang-bang as shown in App. D. In the critical regime I we get an infidelity of about $\mathcal{I}(T) \approx 0.35$ compared to $\mathcal{I}(T) = 0.47$ for a linear protocol whereas in regime II we get $\mathcal{I}(T) \approx 0.15$ versus $\mathcal{I}(T) = 0.22$ for linear. In the low average velocity regime III we get infidelities as low as $\mathcal{I}(T) \approx 0.006$ while linear motion gives $\mathcal{I}(T) = 0.012$.

In regime IV the results show a globally different strategy: in this regime the optimal protocol is to slowly accelerate the Majorana up to some finite velocity and then slowly decelerate back down to the target position. This type of protocol was discussed in earlier work [69, 71] in regimes where there is enough time to accelerate to a moving frame, i.e. regime IV. We note that due to the nearly adiabatic motion in regime IV, the values of infidelity are the lowest $\mathcal{I}(T) \approx \mathcal{O}(10^{-4})$.

We benchmark our results with simulated annealing (SA) on the wall velocity $v_L(t)$ for which the results are shown in Fig. 2(i-l). In this method we iteratively update the velocity $v_L(t)$ by choosing two random intervals of length Δt of which one interval is increased by Δv and the other is decreased by Δv such that the average velocity constraint is preserved. Subsequently the new infidelity \mathcal{I}_i is calculated for the updated velocity and the move is accepted with a probability $e^{-\delta\mathcal{I}/T_{SA}}$ where $\delta\mathcal{I} = \mathcal{I}_i - \mathcal{I}_{i-1}$ is the difference in the infidelity with respect to previous iteration and T_{SA} is the annealing temperature which we slowly cool down to zero.

While we find that SA leads to qualitatively similar strategies as DP and NES, we emphasize that SA is computationally significantly more demanding than NES or DP since a typical SA simulation entails the evaluation of the many-body infidelity for each SA update step. To obtain results with comparable infidelities, the SA simulation requires a total of 100000 evaluations of the infidelity while for DP we only need 440 update steps each involving a single infidelity and gradient evaluation (the latter requiring similar computational complexity as the infidelity calculation); for the NES algorithm we need 50 update steps each with 100 parallelable evaluations to reach convergence.

V. JUMP-MOVE-JUMP [JMJ] MAJORANA CONTROL STRATEGY

The main features of the ML strategies in regimes I, II and III can be encapsulated in a simple model strategy, the jump-move-jump strategy as shown in Fig. 3 a), amenable to semi-analytical and numerical analysis. This strategy consists of two dressed jumps in the position of the domain wall at the beginning and end of the protocol interluded by a period of motion at a constant

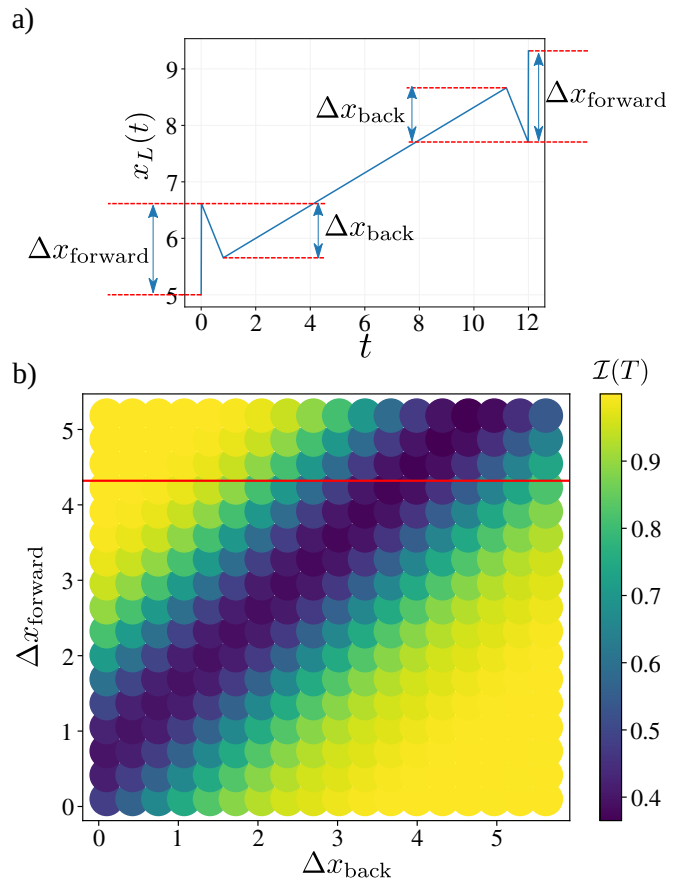


FIG. 3. a) Setup of the ML-inspired simple control strategy consisting of two edge pulses with a forward jump $\Delta x_{\text{forward}}$ and backward jump Δx_{back} together with a constant linear motion in between the dressed jumps. b) Infidelity $\mathcal{I}(T)$ surface plot for the scans over the free parameters $\Delta x_{\text{forward}}$ and Δx_{back} of the model strategy with $\Delta t_{\text{back}} = 0.07w^{-1}$ and $\Delta t_{\text{forward}} = 0.01w^{-1}$ in regime I ($l = 4.32, T = 12$). The red line indicates the line where the size of the forward jump $\Delta x_{\text{forward}}$ is equal to the total movement length l . The parameters of the Majorana control setup are the same as in Fig. 2. The optimal dressed jumps appear at a diagonal set of parameters $\Delta x_{\text{forward}} - \Delta x_{\text{back}} \sim C$ where $C \approx 0.96$. We note that the best protocol has a jump size bigger than the movement length $\Delta x_{\text{forward}} > l$ which means that it jumps over the target position $x_L(T) = x_B$ and then jumps back within the range $x_A < x_L < x_B$ as can be seen in Fig. 1 d) (for regimes I and III).

velocity v . The initial dressed jump comprises an instantaneous forward jump over a distance $\Delta x_{\text{forward}}$ followed by a rapid backward movement over a distance Δx_{back} in a time Δt_{back} . Similarly, the last pulse starts with a rapid backward movement Δx_{back} followed by a forward jump over a distance $\Delta x_{\text{forward}}$. In what follows, we assume that jumps at the beginning and end of the protocol are symmetric and are described by the same parameters.

The simplicity of this model allows us to develop an understanding for the key mechanisms behind the ML strategies and estimate the value of the infidelity of the

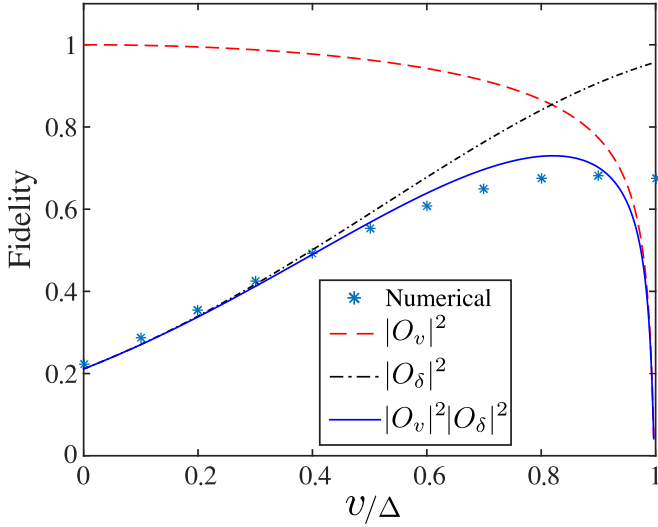


FIG. 4. The jump-move-jump protocol maximizes the product of the two functions O_δ (Eq. 8) and O_v (Eq. 9). Here $l = 4.32$ and $T = 12$ (regime I) and we have used $s = 2.45$ and $\beta = 0.065$. The ground state projection analysis (solid blue) captures the key features of the ML-inspired (one-wall) JMJ strategy (blue stars) for low velocities v but tends to overestimate the penalty for moving at velocities near v_{crit} .

JMJ strategy for a wide range of parameters l, T in regimes I-III (see Fig. 5 and Fig. 3 (b)). In section VA below we will first argue that when we disregard the backward movements, i.e. $\Delta x_{\text{back}} = 0$, the overall strategy can be explained via a trade-off (Fig. 4) between the amount of fidelity loss due to the boundary jumps and the loss due to sudden changes in velocity.

In section VB we also explore how this mechanism can be better controlled with the backward movements $\Delta x_{\text{back}} \neq 0$ which, for a certain subset of parameters $(\Delta x_{\text{forward}}, \Delta x_{\text{back}})$, leads to a model strategy with infidelities that compare competitively with the best ML learned protocols (see the discussion in App. E and Figs. 1 (d) and 2). Our analysis shows that this dressed protocol allows one to better target the ground-state of the system in a moving (constant velocity) frame.

A. Bare Jump-Move-Jump ($\Delta x_{\text{back}} = 0$)

For the case $\Delta x_{\text{back}} = 0$ we minimize the infidelity Eq. 3 with respect to the velocity v of the bulk of the protocol which fixes the instantaneous forward jump to $\Delta x_{\text{forward}} = (l - vT)/2 \equiv \delta$. To make analytic analysis simpler we focus on the case that both the left and the right domain wall positions are being evolved simultaneously with the JMJ strategy. This means that the right wall position x_R in Eq. 2 becomes time-dependent via $x_R(t) = x_L(t) + C_x$ with C_x a fixed constant. This two wall scenario makes it possible to evaluate the strategy in the moving frame basis (App. A), which allows the key rationale behind the JMJ strategy to be revealed.

To evaluate this strategy we expand the infidelity after the first jump $x_L = x_A \mapsto x_L = x_A + \delta$ in terms of the eigenbasis $|\psi_{A+\delta}^i\rangle$ of the Hamiltonian Eq. 1 with the wall at position $x_L = x_A + \delta$ giving

$$\mathcal{I}(T) = 1 - \left| \sum_i \langle \psi_B | U(T) | \psi_{A+\delta}^i \rangle \langle \psi_{A+\delta}^i | \psi_A \rangle \right|^2 \quad (5)$$

in which $U(T) = \mathcal{T}e^{-i \int_0^T H(t) dt}$ is the time-ordered evolution operator with $H(t)$ following the time-dependence of the strategy. We break this equation up into two separate terms

$$\mathcal{I}(T) = 1 - |\langle \psi_B | U(T) | \psi_{A+\delta}^0 \rangle \langle \psi_{A+\delta}^0 | \psi_A \rangle| + \sum_{i>0} |\langle \psi_B | U(T) | \psi_{A+\delta}^i \rangle \langle \psi_{A+\delta}^i | \psi_A \rangle|^2 \quad (6)$$

which allows for an approximate analysis of the separate contributions. Here we focus on the groundstate contribution (first line), making the assumption that the second line is small in comparison.

To approximate the groundstate contribution we insert projections onto the groundstate $|\psi_v^0\rangle$ of a moving frame Hamiltonian $H(v)$ with a velocity v equal to the bulk velocity of the strategy and finally a projection onto the groundstate $|\psi_{B-\delta}^0\rangle$ of the Hamiltonian Eq. 1 with the wall at position $x_L = x_B - \delta$ (just before the final jump) resulting in

$$\mathcal{I}(T) \approx 1 - |\langle \psi_B | \psi_{B-\delta}^0 \rangle \langle \psi_{B-\delta}^0 | \psi_v^0 \rangle \times \langle \psi_v^0 | U(T) | \psi_v^0 \rangle \langle \psi_v^0 | \psi_{A+\delta}^0 \rangle \langle \psi_{A+\delta}^0 | \psi_A \rangle|^2. \quad (7)$$

The $\langle \psi_{A(B)\pm\delta} | \psi_{A(B)} \rangle$ represent the initial and final jumps in position space of size δ which by fitting to our numerical model can be characterized as

$$O_\delta = |\langle \psi_{x_L} | \psi_{x_L+\delta} \rangle|^2 \sim \exp(-\delta^2/s^2) \quad (8)$$

where $s \sim \epsilon + \alpha \lambda_F$ with λ_F the Fermi wavelength and the fitting parameters $(\epsilon, \alpha) = (-0.33, 0.44)$ for one-wall and $(-0.12, 0.3)$ for two-walls when $\Delta = 0.3$.

The amplitude $\langle \psi_v^0 | \psi_{A+\delta}^0 \rangle$ represents the overlap between the static ground state and that of a moving frame with a constant velocity v . We estimate this as follows:

$$O_v = |\langle \psi_{x_L}^0 | \psi_v^0 \rangle|^2 \sim 1 - \beta \left(\frac{v}{\Delta} \right)^2 \gamma \quad (9)$$

with $\gamma = 1/\sqrt{1 - v^2/\Delta^2}$. One way to argue for this form is to use the results of [71] that showed that the energy of the moving frame ground state w.r.t. to the static frame goes as $E \sim \gamma M v^2$ where $M \propto k_F/\Delta$. The overlap can be related to this energy via $O_v \sim 1 - E/k_F \Delta$. We arrive at a value of $\beta \sim 0.13$ by fitting Eq. 9 to moving frame (two-wall) numerical simulations for $v \ll v_{\text{crit}}$. For single wall motion we can calculate value of $\beta \sim 0.065$ by slowly accelerating the wall up to $v \ll v_{\text{crit}}$ and comparing the evolved state with the instantaneous ground-state.

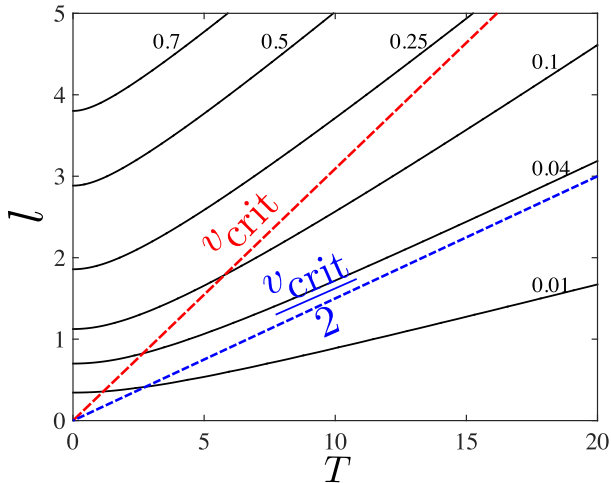


FIG. 5. Contours showing the infidelity \mathcal{I} for the bare (one-wall) jump-move-jump strategy (Eq. 10) as a function of distance l and time T using the same fitted parameters as Fig. 4. The red dashed line indicates when $v_{\text{avg}} = l/T = v_{\text{crit}}$ and the blue dashed line when $v_{\text{avg}} = v_{\text{crit}}/2$, which can be used to distinguish the different Majorana motion regimes as defined in Fig. 1 (c). The jump-move-jump protocol allows for low infidelities even in cases where the average velocity exceeds v_{crit} (regime I).

If we assume a symmetric strategy (e.g. jumps of the same size at the beginning and end) then the fidelity function $\mathcal{F}(T) \approx |O_\delta O_v|^2$ (where $\mathcal{I}(T) = 1 - \mathcal{F}(T)$) to be maximized is approximated as

$$\mathcal{F}(T) \approx \exp\left(-\frac{(l - vT)^2}{2s^2}\right) \times \left[1 - \beta\gamma\left(\frac{v}{\Delta}\right)^2\right]^2 \quad (10)$$

where we have substituted $\delta = (l - vT)/2$. The first function is maximized by making v as large as possible while the second prefers to have small v , with a very severe penalty kicking in as v approaches the critical velocity $\sim \Delta$. In Figure 4 we show how this function behaves for the protocol in regime I, which indicates that the analysis accurately captures the behaviour of the fidelity at small v/Δ but also displays overall qualitative agreement with the numerical results for a wide range of values of v/Δ including the presence of a maximum in the fidelity.

The key to the strategy is the jumps at the beginning and end of the protocol that allow for a constant middle motion at a sub-critical velocity. In Fig. 5 we show how the infidelity behaves for a range of movement lengths l and times T obtained from maximizing Eq. 10 with respect to v . By comparing with Fig. 1 (c) we see that in regime I the bare JMJ strategy gives infidelities of $\mathcal{I}(T) > 0.25$, in regime II (between the dashed lines) about $0.04 < \mathcal{I}(T) < 0.25$ and in the short l -short T regime III (below the blue dashed line) performs particularly well with infidelities $\mathcal{I}(T) \sim \mathcal{O}(10^{-2})$.

This method is only effective however if the jumps

needed are not too large ($l \sim \mathcal{O}(\lambda_F)$). Interestingly, as the overlap behaviour of O_v is relatively unaffected by changes to the chemical potential, this suggests that a chemical potential nearer to the bottom of the band, $\mu \rightarrow -2w$ can help to extend the range of the protocol.

B. Dressed Jump-Move-Jump ($\Delta x_{\text{back}} \neq 0$)

On top of the bare jump-move-jump structure, the ML algorithms dress the protocols with additional forward and backward movements. In this section we will show that the primary purpose behind these additional motions is to better target the moving frame ground state in the *move* part of the *jump-move-jump* protocol.

To proceed we focus on the simple upgraded JMJ protocol that also allows backward motions over distances $\Delta x_{\text{back}} \neq 0$, see Fig. 3 (a). Our first key observation is that the optimal protocols here tend to choose a combined jump size $\Delta x_{\text{forward}} - \Delta x_{\text{back}} \sim C$, see Fig. 3 (b), where C is a fixed constant. This indicates the same primary goal as the JMJ strategy: to allow a period of optimal and roughly constant sub-critical motion.

To understand why the backward motion is a further benefit we examine the instantaneous infidelity in both the static and moving frames for a series of protocols with the fixed bulk velocity v , see Fig. 6 (a). The instantaneous infidelity is defined as $I(t) = 1 - |\langle \psi(t) | \psi_{\text{ins}}^0(t) \rangle|^2$ with $|\psi(t)\rangle = \mathcal{T}e^{-i \int_0^t H(t') dt'} |\psi_A\rangle$ in which $H(t)$ follows the time-dependence of the dressed JMJ strategy and $|\psi_{\text{ins}}^0(t)\rangle$ corresponds to the instantaneous groundstate (at the fixed time t) of the static frame Hamiltonian $\mathcal{H}(t)$ (Eq. 1) or the moving frame Hamiltonian $H_v(t)$ (Eq. A2). The static frame perspective shows that the optimal jump finds a state that slowly becomes the lowest infidelity state after some time. However a more revealing picture emerges if we examine the same set of protocols in a moving frame (inset). Here we see that the objective of the initial jumps is to maximize the overlap with the ground state of the moving frame.

Using the same methodology we can also reveal what moving frame bulk excitations $|\psi_v^i\rangle$ with many-body energy E_v^i (restricting here to single- and two particle excitations only) the dressed protocol occupies during the evolution, see Fig. 6 (b). For protocols close to the bare JMJ strategy (shown in red) one finds that the dominant excitations have energies close to the moving frame bulk gap ($E_v^i \approx 0.08$). The dressed jumps (in blue and green) however are able to lower the amplitudes of these excitations, but at the cost of also exciting some higher energy quasi-particles. For dressed jumps that are too large (in green) these higher energy excitations eventually dominate and one gets an increase in the ground state infidelity.

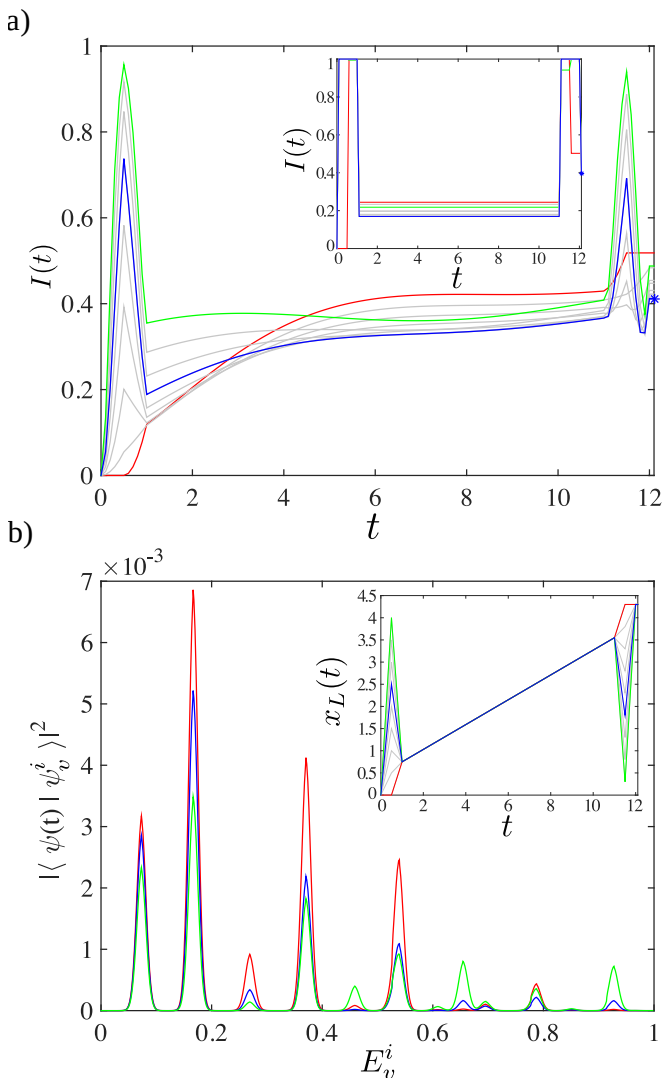


FIG. 6. a) Instantaneous Infidelity $I(t)$ with respect to the static (lab) frame groundstate (main panel) and moving frame groundstate (inset) as a function of the protocol time t for various dressed jumps in regime I which are depicted by the different colours (red,blue,green,grey) and shown in the inset of b). The optimal dressed jump (blue) has the minimum infidelity with the moving frame groundstate and becomes the strategy with the minimum static frame infidelity after about $t \approx 4$. b) The time-evolved state $|\psi(t)\rangle$ expanded in the single and two particle excitations $|\psi_v^i\rangle$ of the moving frame basis with energies E_v^i at $t = T/2$ for a forward jump (red), an optimal dressed jump (blue) and non-optimal dressed jump (green) for regime I as given in the inset. The occupation probabilities (delta functions) are convoluted for visualisation purposes. The forward jump strategy (red) occupies the excitations close to the bottom of the band in the moving frame ($E_v^i \approx 0.08$) more compared to the dressed jumps (blue and green). In this figure all times are in units of $1/\omega$.

VI. CONCLUSION AND FURTHER WORK

We have applied two state-of-the-art machine learning techniques, namely differentiable programming (DP) and natural evolution strategies (NES), to the problem of manipulating Majorana bound-states in a topological superconductor. For DP we have shown that the entire dynamical evolution of any free-fermion system can be functionally differentiated, allowing for more efficient optimization protocols. This in turn provides an ability to tackle computationally harder problems and allows the dynamical optimization to be integrated seamlessly with both direct and Neural-Network parameterizations of quantum control protocols.

In addition to this we have shown how the Majorana control problem itself can be naturally formulated as a game. This allows the application of reinforcement learning approaches and NES to zero-mode manipulation. The key advantage here is both speed and flexibility compared to, e.g., the standard MC methods such as simulated annealing. Beyond the advantages observed in our numerical experiments there are a number of additional conceptual and practical ingredients which can be taken advantage of in the reinforcement learning setup including a flexible exploration step, delayed rewards, partial observations, and the ease of accounting for the stochastic nature of the reward function, all of which may be particularly relevant to experimental setups.

Note that these RL approaches are not specific to Majorana bound state control, and could also be applied to different dynamical many-body problems with radically different motivations and cost functions (e.g. log-likelihood [108], Fisher information [109] or the trace distance [110]).

On the theoretical level we have introduced a framework for dividing up the Majorana control problem into four distinct transport regimes. This has deepened the understanding of the problem and help to establish a connection with optimal control theory more broadly. Remarkably our numerical simulations displayed an innate awareness of this rich landscape and uncovered important hidden aspects of the underlying physics. In particular they have identified a new class of protocol that radically outperform other known strategies (adiabatic and bang-bang) when there are both spatial and temporal constraints.

The core of this alternative strategy is a sudden jump followed by a period of constant velocity motion and then another jump (JMJ). A theoretical analysis of this dynamics shows that the strategy simultaneously exploits the models stability at constant velocities below a certain threshold, and the property that small instantaneous changes in the domain wall position do not dramatically reduce the ground state fidelity. Further analysis of dressed JMJ protocols reveals that more complex initial jump sequences can, in addition to allowing a sub-critical velocity, better target the ground state of the moving frame. The protocol resembles the parallel

recent development of the Bang-Anneal-Bang protocols [91] for ground state preparation in Noisy Intermediate Scale Quantum devices. Our theoretical analysis illuminates why this type of strategy works so successfully and we are hopeful that this approach will motivate more general theoretical analysis of related protocols.

Another natural direction to explore is the application of our methods to the problem of Majorana braiding, which is the ultimate goal behind the study and control of zero-modes in the context of topological quantum computing. Of course, in the space between our theoretical toy-model setup and the actual topological quantum devices there are many additional layers of complexity and it is an interesting open question which aspects of our protocols remain robust. We emphasize however that the strength of the RL setup is that one can easily encode other experimental restrictions on the control by including them in the reward or action spaces [111]. As such the application of these methods can be readily extended to other more complicated models, such as models including the effect of interactions [112], and simulation techniques, such as time-dependent density-matrix renormalization group [113].

In a broader sense we believe our work shows that machine learning for quantum control can be done at a scale,

speed, and precision that is relevant to modern experimental devices. As such we believe that it will be used to overcome obstacles to realizing large-scale quantum computation, quantum communication networks, quantum thermal machines, analogue quantum simulations, and control of other quantum many-body dynamical systems more broadly.

ACKNOWLEDGMENTS

We would like to thank Andreas Buchleitner, Steve Campbell, Aaron Conlon, Shane Dooley, Ian Jubb, Kevin Kavanagh, Jinguo Liu, Xiuzhe Luo, Jiayu Shen and Lei Wang for helpful discussions regarding this project. L.C and G.K. acknowledge Science Foundation Ireland for financial support through Career Development Award 15/CDA/3240. G. K. was also supported by a Schrödinger Fellowship. J.C. acknowledges support from Natural Sciences and Engineering Research Council of Canada (NSERC), the Shared Hierarchical Academic Research Computing Network (SHARCNET), Compute Canada, Google Quantum Research Award, and the Canadian Institute for Advanced Research (CIFAR) AI chair program. D.L and BKC acknowledge support from the Department of Energy grant DOE desc0020165.

-
- [1] Jay M. Gambetta, Jerry M. Chow, and Matthias Steffen, “Building logical qubits in a superconducting quantum computing system,” *npj Quantum Information* **3**, 2 (2017).
 - [2] J. I. Cirac and P. Zoller, “Quantum computations with cold trapped ions,” *Phys. Rev. Lett.* **74**, 4091–4094 (1995).
 - [3] Justin G. Bohnet, Brian C. Sawyer, Joseph W. Britton, Michael L. Wall, Ana Maria Rey, Michael Foss-Feig, and John J. Bollinger, “Quantum spin dynamics and entanglement generation with hundreds of trapped ions,” *Science* **352**, 1297–1301 (2016).
 - [4] Colin D. Bruzewicz, John Chiaverini, Robert McConnell, and Jeremy M. Sage, “Trapped-ion quantum computing: Progress and challenges,” *Applied Physics Reviews* **6**, 021314 (2019), <https://doi.org/10.1063/1.5088164>.
 - [5] Christian Gross and Immanuel Bloch, “Quantum simulations with ultracold atoms in optical lattices,” *Science* **357**, 995–1001 (2017).
 - [6] Brian B. Zhou, Alexandre Baksic, Hugo Ribeiro, Christopher G. Yale, F. Joseph Heremans, Paul C. Jerger, Adrian Auer, Guido Burkard, Aashish A. Clerk, and David D. Awschalom, “Accelerated quantum control using superadiabatic dynamics in a solid-state lambda system,” *Nature Physics* **13**, 330–334 (2017).
 - [7] Francesco Casola, Toeno van der Sar, and Amir Yacoby, “Probing condensed matter physics with magnetometry based on nitrogen-vacancy centres in diamond,” *Nature Reviews Materials* **3**, 17088 (2018).
 - [8] David P. DiVincenzo, “The physical implementation of quantum computation,” *Fortschritte der Physik* **48**, 771–783 (2000).
 - [9] Alexandre Baksic, Hugo Ribeiro, and Aashish A. Clerk, “Speeding up adiabatic quantum state transfer by using dressed states,” *Phys. Rev. Lett.* **116**, 230503 (2016).
 - [10] Herschel Rabitz, Regina de Vivie-Riedle, Marcus Motzkus, and Karl Kompa, “Whither the future of controlling quantum phenomena?” *Science* **288**, 824–828 (2000).
 - [11] Xiaoting Wang, Michele Allegra, Kurt Jacobs, Seth Lloyd, Cosmo Lupo, and Masoud Mohseni, “Quantum brachistochrone curves as geodesics: Obtaining accurate minimum-time protocols for the control of quantum systems,” *Phys. Rev. Lett.* **114**, 170501 (2015).
 - [12] D. Guéry-Odelin, A. Ruschhaupt, A. Kiely, E. Torrontegui, S. Martínez-Garaot, and J. G. Muga, “Shortcuts to adiabaticity: Concepts, methods, and applications,” *Rev. Mod. Phys.* **91**, 045001 (2019).
 - [13] A. del Campo and K. Sengupta, “Controlling quantum critical dynamics of isolated systems,” *The European Physical Journal Special Topics* **224**, 189–203 (2015).
 - [14] A. G. J. MacFarlane, Jonathan P. Dowling, and Gerard J. Milburn, “Quantum technology: The second quantum revolution,” *Philosophical Transactions of the Royal Society of London. Series A: Mathematical, Physical and Engineering Sciences* **361**, 1655–1674 (2003).
 - [15] Liang Fu and C. L. Kane, “Superconducting proximity effect and majorana fermions at the surface of a topological insulator,” *Phys. Rev. Lett.* **100**, 096407 (2008).
 - [16] Roman M. Lutchyn, Jay D. Sau, and S. Das Sarma, “Majorana fermions and a topological phase tran-

- sition in semiconductor-superconductor heterostructures,” *Phys. Rev. Lett.* **105**, 077001 (2010).
- [17] Yuval Oreg, Gil Refael, and Felix von Oppen, “Helical liquids and majorana bound states in quantum wires,” *Phys. Rev. Lett.* **105**, 177002 (2010).
- [18] Jason Alicea, Yuval Oreg, Gil Refael, Felix von Oppen, and Matthew P. A. Fisher, “Non-abelian statistics and topological quantum information processing in 1d wire networks,” *Nature Physics* **7**, 412–417 (2011).
- [19] Morten Kjaergaard, Konrad Wölms, and Karsten Flensberg, “Majorana fermions in superconducting nanowires without spin-orbit coupling,” *Phys. Rev. B* **85**, 020503 (2012).
- [20] Martin Leijnse and Karsten Flensberg, “Introduction to topological superconductivity and majorana fermions,” *Semiconductor Science and Technology* **27**, 124003 (2012).
- [21] V. Mourik, K. Zuo, S. M. Frolov, S. R. Plissard, E. P. A. M. Bakkers, and L. P. Kouwenhoven, “Signatures of majorana fermions in hybrid superconductor-semiconductor nanowire devices,” *Science* **336**, 1003–1007 (2012).
- [22] M. T. Deng, C. L. Yu, G. Y. Huang, M. Larsson, P. Caroff, and H. Q. Xu, “Anomalous zero-bias conductance peak in a nb-insb nanowire-nb hybrid device,” *Nano Letters* **12**, 6414–6419 (2012).
- [23] Anindya Das, Yuval Ronen, Yonatan Most, Yuval Oreg, Moty Heiblum, and Hadas Shtrikman, “Zero-bias peaks and splitting in an al-inas nanowire topological superconductor as a signature of majorana fermions,” *Nature Physics* **8**, 887–895 (2012).
- [24] Hao Zhang, Chun-Xiao Liu, Sasa Gazibegovic, Di Xu, John A. Logan, Guanzhong Wang, Nick van Loo, Jouri D. S. Bommer, Michiel W. A. de Moor, Diana Car, Roy L. M. Op het Veld, Petrus J. van Veldhoven, Sebastian Koelling, Marcel A. Verheijen, Mihir Pendharkar, Daniel J. Pennachio, Borzoyeh Shojaei, Joon Sue Lee, Chris J. Palmstrøm, Erik P. A. M. Bakkers, S. Das Sarma, and Leo P. Kouwenhoven, “Quantized majorana conductance,” *Nature* **556**, 74–79 (2018).
- [25] A Yu Kitaev, “Unpaired majorana fermions in quantum wires,” *Physics-Uspekhi* **44**, 131–136 (2001).
- [26] A.Yu. Kitaev, “Fault-tolerant quantum computation by anyons,” *Annals of Physics* **303**, 2 – 30 (2003).
- [27] Sankar Das Sarma, Michael Freedman, and Chetan Nayak, “Majorana zero modes and topological quantum computation,” *npj Quantum Information* **1**, 1–13 (2015).
- [28] Chetan Nayak, Steven H. Simon, Ady Stern, Michael Freedman, and Sankar Das Sarma, “Non-abelian anyons and topological quantum computation,” *Rev. Mod. Phys.* **80**, 1083–1159 (2008).
- [29] T D Stanescu and S Tewari, “Majorana fermions in semiconductor nanowires: fundamentals, modeling, and experiment,” *Journal of Physics: Condensed Matter* **25**, 233201 (2013).
- [30] David Aasen, Michael Hell, Ryan V. Mishmash, Andrew Higginbotham, Jeroen Danon, Martin Leijnse, Thomas S. Jespersen, Joshua A. Folk, Charles M. Marcus, Karsten Flensberg, and Jason Alicea, “Milestones toward majorana-based quantum computing,” *Phys. Rev. X* **6**, 031016 (2016).
- [31] Diego Rainis and Daniel Loss, “Majorana qubit decoherence by quasiparticle poisoning,” *Phys. Rev. B* **85**, 174533 (2012).
- [32] Athanasios Voulodimos, Nikolaos Doulamis, Anastasios Doulamis, and Eftychios Protopapadakis, “Deep Learning for Computer Vision: A Brief Review,” *Computational Intelligence and Neuroscience* **2018**, 7068349 (2018).
- [33] Tom Young, Devamanyu Hazarika, Soujanya Poria, and Erik Cambria, “Recent Trends in Deep Learning Based Natural Language Processing,” arXiv:1708.02709 [cs] (2018), arXiv:1708.02709 [cs].
- [34] Gökçen Eraslan, Žiga Avsec, Julien Gagneur, and Fabian J. Theis, “Deep learning: New computational modelling techniques for genomics,” *Nature Reviews Genetics* **20**, 389–403 (2019).
- [35] Giuseppe Carleo, Ignacio Cirac, Kyle Cranmer, Laurent Daudet, Maria Schuld, Naftali Tishby, Leslie Vogt-Maranto, and Lenka Zdeborová, “Machine learning and the physical sciences,” *Rev. Mod. Phys.* **91**, 045002 (2019).
- [36] Juan Carrasquilla, “Machine learning for quantum matter,” *Advances in Physics: X* **5**, 1797528 (2020).
- [37] I. E. Lagaris, A. Likas, and D. I. Fotiadis, “Artificial neural network methods in quantum mechanics,” *Computer Physics Communications* **104**, 1–14 (1997).
- [38] Juan Carrasquilla and Roger G. Melko, “Machine learning phases of matter,” *Nature Physics* **13**, 431–434 (2017).
- [39] Giuseppe Carleo and Matthias Troyer, “Solving the quantum many-body problem with artificial neural networks,” *Science* **355**, 602–606 (2017).
- [40] Dmitrii Kochkov and Bryan K Clark, “Variational optimization in the ai era: Computational graph states and supervised wave-function optimization,” arXiv preprint arXiv:1811.12423 (2018).
- [41] Di Luo and Bryan K. Clark, “Backflow transformations via neural networks for quantum many-body wave functions,” *Phys. Rev. Lett.* **122**, 226401 (2019).
- [42] David Pfau, James S. Spencer, Alexander G. de G. Matthews, and W. M. C. Foulkes, “Ab-initio solution of the many-electron schrödinger equation with deep neural networks,” (2019), arXiv:1909.02487 [physics.chem-ph].
- [43] Jan Hermann, Zeno Schtzle, and Frank No, “Deep neural network solution of the electronic schrödinger equation,” (2019), arXiv:1909.08423 [physics.comp-ph].
- [44] Or Sharir, Yoav Levine, Noam Wies, Giuseppe Carleo, and Amnon Shashua, “Deep autoregressive models for the efficient variational simulation of many-body quantum systems,” *Phys. Rev. Lett.* **124**, 020503 (2020).
- [45] Mohamed Hibat-Allah, Martin Ganahl, Lauren E. Hayward, Roger G. Melko, and Juan Carrasquilla, “Recurrent neural network wave functions,” *Phys. Rev. Research* **2**, 023358 (2020).
- [46] Sirui Lu, Xun Gao, and L.-M. Duan, “Efficient representation of topologically ordered states with restricted boltzmann machines,” *Phys. Rev. B* **99**, 155136 (2019).
- [47] Xun Gao and Lu-Ming Duan, “Efficient representation of quantum many-body states with deep neural networks,” *Nature Communications* **8**, 662 (2017).
- [48] Ivan Glasser, Nicola Pancotti, Moritz August, Ivan D. Rodriguez, and J. Ignacio Cirac, “Neural-network quantum states, string-bond states, and chiral topological states,” *Physical Review X* **8** (2018), 10.1103/physrevx.8.011006.

- [49] Giacomo Torlai, Guglielmo Mazzola, Juan Carrasquilla, Matthias Troyer, Roger Melko, and Giuseppe Carleo, “Neural-network quantum state tomography,” *Nature Physics* **14**, 447 (2018).
- [50] Giacomo Torlai and Roger G. Melko, “Latent Space Purification via Neural Density Operators,” *Physical Review Letters* **120**, 240503 (2018).
- [51] Juan Carrasquilla, Giacomo Torlai, Roger G. Melko, and Leandro Aolita, “Reconstructing quantum states with generative models,” *Nature Machine Intelligence* **1**, 155 (2019).
- [52] Matthias Rupp, Alexandre Tkatchenko, Klaus-Robert Müller, and O. Anatole von Lilienfeld, “Fast and accurate modeling of molecular atomization energies with machine learning,” *Phys. Rev. Lett.* **108**, 058301 (2012).
- [53] Matthias Rupp, “Machine learning for quantum mechanics in a nutshell,” *International Journal of Quantum Chemistry* **115**, 1058–1073 (2015).
- [54] K. T. Schütt, M. Gastegger, A. Tkatchenko, K.-R. Müller, and R. J. Maurer, “Unifying machine learning and quantum chemistry with a deep neural network for molecular wavefunctions,” *Nature Communications* **10**, 5024 (2019).
- [55] John C. Snyder, Matthias Rupp, Katja Hansen, Klaus-Robert Müller, and Kieron Burke, “Finding density functionals with machine learning,” *Phys. Rev. Lett.* **108**, 253002 (2012).
- [56] Li Li, John C. Snyder, Isabelle M. Pelaschier, Jessica Huang, Uma-Naresh Niranjana, Paul Duncan, Matthias Rupp, Klaus-Robert Müller, and Kieron Burke, “Understanding machine-learned density functionals,” *International Journal of Quantum Chemistry* **116**, 819–833 (2016).
- [57] Junwei Liu, Yang Qi, Zi Yang Meng, and Liang Fu, “Self-learning monte carlo method,” *Phys. Rev. B* **95**, 041101 (2017).
- [58] Li Huang and Lei Wang, “Accelerated monte carlo simulations with restricted boltzmann machines,” *Phys. Rev. B* **95**, 035105 (2017).
- [59] S. Pilati, E. M. Inack, and P. Pieri, “Self-learning projective quantum monte carlo simulations guided by restricted boltzmann machines,” *Phys. Rev. E* **100**, 043301 (2019).
- [60] Vedran Dunjko and Hans J. Briegel, “Machine learning & artificial intelligence in the quantum domain: A review of recent progress,” *Reports on Progress in Physics* **81**, 074001 (2018).
- [61] Marin Bukov, Alexandre G. R. Day, Dries Sels, Phillip Weinberg, Anatoli Polkovnikov, and Pankaj Mehta, “Reinforcement learning in different phases of quantum control,” *Phys. Rev. X* **8**, 031086 (2018).
- [62] Murphy Yuezhen Niu, Sergio Boixo, Vadim N. Smelyanskiy, and Hartmut Neven, “Universal quantum control through deep reinforcement learning,” *npj Quantum Information* **5**, 1–8 (2019).
- [63] Frank Schfer, Michal Kloc, Christoph Bruder, and Niels Lrch, “A differentiable programming method for quantum control,” *Machine Learning: Science and Technology* (2020), 10.1088/2632-2153/ab9802.
- [64] Volodymyr Mnih, Koray Kavukcuoglu, David Silver, Andrei A. Rusu, Joel Veness, Marc G. Bellemare, Alex Graves, Martin Riedmiller, Andreas K. Fidjeland, Georg Ostrovski, Stig Petersen, Charles Beattie, Amir Sadik, Ioannis Antonoglou, Helen King, Dharmashan Kumar, Daan Wierstra, Shane Legg, and Demis Hassabis, “Human-level control through deep reinforcement learning,” *Nature* **518**, 529–533 (2015).
- [65] David Silver, Aja Huang, Chris J. Maddison, Arthur Guez, Laurent Sifre, George van den Driessche, Julian Schrittwieser, Ioannis Antonoglou, Veda Panneerselvam, Marc Lanctot, Sander Dieleman, Dominik Grewe, John Nham, Nal Kalchbrenner, Ilya Sutskever, Timothy Lillicrap, Madeleine Leach, Koray Kavukcuoglu, Thore Graepel, and Demis Hassabis, “Mastering the game of Go with deep neural networks and tree search,” *Nature* **529**, 484–489 (2016).
- [66] Richard S. Sutton and Andrew G. Barto, *Reinforcement Learning: An Introduction* (A Bradford Book, Cambridge, MA, USA, 2018).
- [67] Atılım Günes Baydin, Barak A. Pearlmutter, Alexey Andreyevich Radul, and Jeffrey Mark Siskind, “Automatic differentiation in machine learning: A survey,” *J. Mach. Learn. Res.* **18**, 55955637 (2017).
- [68] Ingo Rechenberg, *Evolutionsstrategie: Optimierung technischer Systeme nach Prinzipien der biologischen Evolution* (Stuttgart : Frommann-Holzboog, 1973).
- [69] M. S. Scheurer and A. Shnirman, “Nonadiabatic processes in majorana qubit systems,” *Phys. Rev. B* **88**, 064515 (2013).
- [70] Torsten Karzig, Armin Rahmani, Felix von Oppen, and Gil Refael, “Optimal control of majorana zero modes,” *Phys. Rev. B* **91**, 201404 (2015).
- [71] A. Conlon, D. Pellegrino, J. K. Slingerland, S. Doolley, and G. Kells, “Error generation and propagation in majorana-based topological qubits,” *Phys. Rev. B* **100**, 134307 (2019).
- [72] Piet W. Brouwer, Mathias Duckheim, Alessandro Romito, and Felix von Oppen, “Topological superconducting phases in disordered quantum wires with strong spin-orbit coupling,” *Phys. Rev. B* **84**, 144526 (2011).
- [73] Suk Bum Chung, Hai-Jun Zhang, Xiao-Liang Qi, and Shou-Cheng Zhang, “Topological superconducting phase and majorana fermions in half-metal/superconductor heterostructures,” *Phys. Rev. B* **84**, 060510 (2011).
- [74] S. Nadj-Perge, I. K. Drozdov, B. A. Bernevig, and Ali Yazdani, “Proposal for realizing majorana fermions in chains of magnetic atoms on a superconductor,” *Phys. Rev. B* **88**, 020407 (2013).
- [75] B.A. Bernevig and T.L. Hughes, *Topological Insulators and Topological Superconductors* (Princeton University Press, 2013).
- [76] N. Read and Dmitry Green, “Paired states of fermions in two dimensions with breaking of parity and time-reversal symmetries and the fractional quantum hall effect,” *Phys. Rev. B* **61**, 10267–10297 (2000).
- [77] D. A. Ivanov, “Non-abelian statistics of half-quantum vortices in p -wave superconductors,” *Phys. Rev. Lett.* **86**, 268–271 (2001).
- [78] Ady Stern, Felix von Oppen, and Eros Mariani, “Geometric phases and quantum entanglement as building blocks for non-abelian quasiparticle statistics,” *Phys. Rev. B* **70**, 205338 (2004).
- [79] Michael Stone and Suk-Bum Chung, “Fusion rules and vortices in $p_x + ip_y$ superconductors,” *Phys. Rev. B* **73**, 014505 (2006).
- [80] Jan Carl Budich, Stefan Walter, and Björn Trauzettel, “Failure of protection of majorana based qubits against

- decoherence,” *Phys. Rev. B* **85**, 121405 (2012).
- [81] François Konschelle and Fabian Hassler, “Effects of nonequilibrium noise on a quantum memory encoded in majorana zero modes,” *Phys. Rev. B* **88**, 075431 (2013).
- [82] H. T. Ng, “Decoherence of interacting majorana modes,” *Scientific Reports* **5**, 12530 (2015).
- [83] Fabio L. Pedrocchi and David P. DiVincenzo, “Majorana braiding with thermal noise,” *Phys. Rev. Lett.* **115**, 120402 (2015).
- [84] Ying Hu, Zi Cai, Mikhail A. Baranov, and Peter Zoller, “Majorana fermions in noisy kitaev wires,” *Phys. Rev. B* **92**, 165118 (2015).
- [85] Christina Knapp, Torsten Karzig, Roman M. Lutchyn, and Chetan Nayak, “Dephasing of majorana-based qubits,” *Phys. Rev. B* **97**, 125404 (2018).
- [86] Erik Torrontegui, Sara Ibáñez, Sofia Martínez-Garaot, Michele Modugno, Adolfo del Campo, David Guéry-Odelin, Andreas Ruschhaupt, Xi Chen, and Juan Gonzalo Muga, “Chapter 2 - Shortcuts to Adiabaticity,” in *Advances In Atomic, Molecular, and Optical Physics*, Advances in Atomic, Molecular, and Optical Physics, Vol. 62, edited by Ennio Arimondo, Paul R. Berman, and Chun C. Lin (Academic Press, 2013) pp. 117–169.
- [87] Torsten Karzig, Falko Pientka, Gil Refael, and Felix von Oppen, “Shortcuts to non-abelian braiding,” *Phys. Rev. B* **91**, 201102 (2015).
- [88] Torsten Karzig, Gil Refael, and Felix von Oppen, “Boosting majorana zero modes,” *Phys. Rev. X* **3**, 041017 (2013).
- [89] Bela Bauer, Torsten Karzig, Ryan V. Mishmash, Andrey E. Antipov, and Jason Alicea, “Dynamics of Majorana-based qubits operated with an array of tunable gates,” *SciPost Phys.* **5**, 4 (2018).
- [90] Zhi-Cheng Yang, Armin Rahmani, Alireza Shabani, Hartmut Neven, and Claudio Chamon, “Optimizing variational quantum algorithms using pontryagin’s minimum principle,” *Phys. Rev. X* **7**, 021027 (2017).
- [91] Lucas T. Brady, Christopher L. Baldwin, Aniruddha Bapat, Yaroslav Kharkov, and Alexey V. Gorshkov, “Optimal protocols in quantum annealing and qaoa problems,” (2020), [arXiv:2003.08952 \[quant-ph\]](https://arxiv.org/abs/2003.08952).
- [92] Michael Victor Berry, “Quantum phase corrections from adiabatic iteration,” *Proceedings of the Royal Society of London. A. Mathematical and Physical Sciences* **414**, 31–46 (1987).
- [93] Michal Deschamps, Gwendal Kervern, Dominique Massiot, Guido Pintacuda, Lyndon Emsley, and Philip J. Grandinetti, “Superadiabaticity in magnetic resonance,” *The Journal of Chemical Physics* **129**, 204110 (2008), <https://doi.org/10.1063/1.3012356>.
- [94] Luuk Coopmans, Di Luo, Graham Kells, Bryan K. Clark, and Juan Carrasquilla, “Protocol discovery for the quantum control of majoranas by differential programming and natural evolution strategies, github repository,” (2020).
- [95] R. E. Wengert, “A simple automatic derivative evaluation program,” *Commun. ACM* **7**, 463464 (1964).
- [96] Hai-Jun Liao, Jin-Guo Liu, Lei Wang, and Tao Xiang, “Differentiable programming tensor networks,” *Phys. Rev. X* **9**, 031041 (2019).
- [97] Hao Xie, Jin-Guo Liu, and Lei Wang, “Automatic differentiation of dominant eigensolver and its applications in quantum physics,” *Phys. Rev. B* **101**, 245139 (2020).
- [98] Sandro Sorella and Luca Capriotti, “Algorithmic differentiation and the calculation of forces by quantum monte carlo,” *The Journal of Chemical Physics* **133**, 234111 (2010).
- [99] Shi-Xin Zhang, Zhou-Quan Wan, and Hong Yao, “Automatic differentiable monte carlo: Theory and application,” (2019), [arXiv:1911.09117 \[physics.comp-ph\]](https://arxiv.org/abs/1911.09117).
- [100] Nelson Leung, Mohamed Abdelhafez, Jens Koch, and David Schuster, “Speedup for quantum optimal control from automatic differentiation based on graphics processing units,” *Phys. Rev. A* **95**, 042318 (2017).
- [101] David E. Rumelhart, Geoffrey E. Hinton, and Ronald J. Williams, “Learning representations by back-propagating errors,” *Nature* **323**, 533–536 (1986).
- [102] James Bradbury, Roy Frostig, Peter Hawkins, Matthew James Johnson, Chris Leary, Dougal Maclaurin, and Skye Wanderman-Milne, “JAX: composable transformations of Python+NumPy programs,” (2018).
- [103] H.-P Schwefel, *Numerische Optimierung von Computer-Modellen mittels der Evolutionsstrategie*, ISR, Vol. 26 (Birkhaeuser, Basel/Stuttgart, 1977) p. 390.
- [104] Daan Wierstra, Tom Schaul, Tobias Glasmachers, Yi Sun, Jan Peters, and Jürgen Schmidhuber, “Natural evolution strategies,” *Journal of Machine Learning Research* **15**, 949–980 (2014).
- [105] Tim Salimans, Jonathan Ho, Xi Chen, Szymon Sidor, and Ilya Sutskever, “Evolution Strategies as a Scalable Alternative to Reinforcement Learning,” [arXiv:1703.03864 \[cs, stat\]](https://arxiv.org/abs/1703.03864) (2017), [arXiv:1703.03864 \[cs, stat\]](https://arxiv.org/abs/1703.03864).
- [106] Richard S. Sutton and Andrew G. Barto, *Reinforcement Learning: An Introduction*, 2nd ed. (The MIT Press, 2018).
- [107] Diederik P. Kingma and Jimmy Ba, “Adam: A method for stochastic optimization,” in *3rd International Conference on Learning Representations, ICLR 2015, San Diego, CA, USA, May 7-9, 2015, Conference Track Proceedings*, edited by Yoshua Bengio and Yann LeCun (2015).
- [108] Christopher M. Bishop, *Pattern Recognition and Machine Learning (Information Science and Statistics)* (Springer-Verlag, Berlin, Heidelberg, 2006).
- [109] D. Petz and C. Ghinea, “Introduction to quantum fisher information,” in *Quantum Probability and Related Topics*, Vol. Volume 27 (WORLD SCIENTIFIC, 2011) pp. 261–281.
- [110] Michael A. Nielsen and Isaac L. Chuang, *Quantum Computation and Quantum Information: 10th Anniversary Edition*, 10th ed. (Cambridge University Press, New York, NY, USA, 2011).
- [111] C. Liu, X. Xu, and D. Hu, “Multiobjective reinforcement learning: A comprehensive overview,” *IEEE Transactions on Systems, Man, and Cybernetics: Systems* **45**, 385–398 (2015).
- [112] E. M. Stoudenmire, Jason Alicea, Oleg A. Starykh, and Matthew P.A. Fisher, “Interaction effects in topological superconducting wires supporting majorana fermions,” *Phys. Rev. B* **84**, 014503 (2011).
- [113] Steven R. White and Adrian E. Feiguin, “Real-time evolution using the density matrix renormalization group,” *Phys. Rev. Lett.* **93**, 076401 (2004).
- [114] Jun John Sakurai, *Modern quantum mechanics; rev. ed.* (Addison-Wesley, Reading, MA, 1994).
- [115] P. Ring and P. Schuck, *The Nuclear Many-Body Prob-*

- lem*, Physics and astronomy online library (Springer, 2004).
- [116] Mike B. Giles, “Collected matrix derivative results for forward and reverse mode algorithmic differentiation,” in *Advances in Automatic Differentiation*, edited by Christian H. Bischof, H. Martin Bücker, Paul Hovland, Uwe Naumann, and Jean Utke (Springer Berlin Heidelberg, Berlin, Heidelberg, 2008) pp. 35–44.

Appendix

Protocol Discovery for the Quantum Control of Majoranas by Differential Programming and Natural Evolution Strategies

Appendix A: Derivation of the Critical Velocity and Moving Frame Picture

In this appendix we first introduce some background theory related to the critical velocity and the Majorana-mode wave function in the moving frame. Afterwards we derive the resonance time scale T_{res} for Majorana shuttling from the Fermi golden rule and finally we show the emergence of this resonance timescale in numerical simulations for forward oscillating motion.

1. Dispersion and Majorana Mode in the Moving Frame

To find the critical velocity we start from the periodic ($N+1=1$) Kitaev chain Hamiltonian (Eq. 1 with $V(x, t) = 0$) in the continuum which reads after a Fourier transformation

$$H_k = \vec{d}_k \cdot \vec{\sigma} = \begin{pmatrix} \frac{k^2}{2m} - \mu & i\Delta k \\ -i\Delta k & -\frac{k^2}{2m} + \mu \end{pmatrix} \quad (\text{A1})$$

with $\vec{d}_k = (0, -\Delta k, \frac{k^2}{2m} - \mu)$, momentum k and $\vec{\sigma}$ the Pauli spin matrices. Solving for the energy eigenvalues gives mode dispersion $\epsilon_k = \pm \left| \vec{d}_k \right| = \pm \sqrt{(\frac{k^2}{2m} - \mu)^2 + \Delta^2 k^2}$.

The moving frame can now be obtained by a Galilean transformation in terms of the unitary rotation $U(t) = e^{-ik \int_0^t v(t') dt'}$ which is the time dependent translation operator that rotates to a frame with domain wall velocity $v(t)$. Applying this to A1 gives the moving frame Hamiltonian

$$H_v(t) = U^\dagger(t) H_k U(t) + i \frac{dU^\dagger}{dt} U(t) = \begin{pmatrix} \frac{k^2}{2m} - \mu + v(t)k & i\Delta k \\ -i\Delta k & -\frac{k^2}{2m} + \mu + v(t)k \end{pmatrix}. \quad (\text{A2})$$

The moving frame has an extra term $v(t)k$ on the diagonal which means the moving frame energy dispersion is $\epsilon_k = \pm \left| \vec{d}_k \right| = \pm \sqrt{(\frac{k^2}{2m} - \mu)^2 + \Delta^2 k^2 + vk}$ [69]. This results in a tilted dispersion as shown in Fig. A1, when $v = \Delta$ the tilt causes the gap to close and we have a topological phase transition. This velocity defines the critical velocity $v_{\text{crit}} = \Delta$.

Besides the energy dispersion, we can also look at the wave function of the Majorana zero modes in the moving frame. To find this wave function we solve for the zero-energy solutions of the moving frame Hamiltonian A2 which results in $\psi = [\phi, -\phi]^\top$ with

$$\phi(x) \propto e^{-x/(\gamma\xi)} \sin\left(\sqrt{k_F^2 + 1/(\gamma\xi)^2} x\right). \quad (\text{A3})$$

The difference with the Majoranas in the lab frame is that the localization length $\xi = 1/\Delta m$ is dilated by a factor $\gamma = 1/\sqrt{1 - \frac{v^2}{\Delta^2}}$ causing the Majorana modes to become spatially more extended (delocalized) in the moving frame. When $v = v_{\text{crit}} = \Delta$ the localization length becomes infinite indicating that the local character is lost and hence a topological phase transition occurs as shown in Fig. A1.

2. Derivation and numerical analysis of the resonant time scale

To derive the time scale for resonant Majorana motion we consider a scenario in which we are shuttling the left Majorana back and forth by using

$$v_L(t) = v_{\text{max}} \sin \omega t \quad (\text{A4})$$

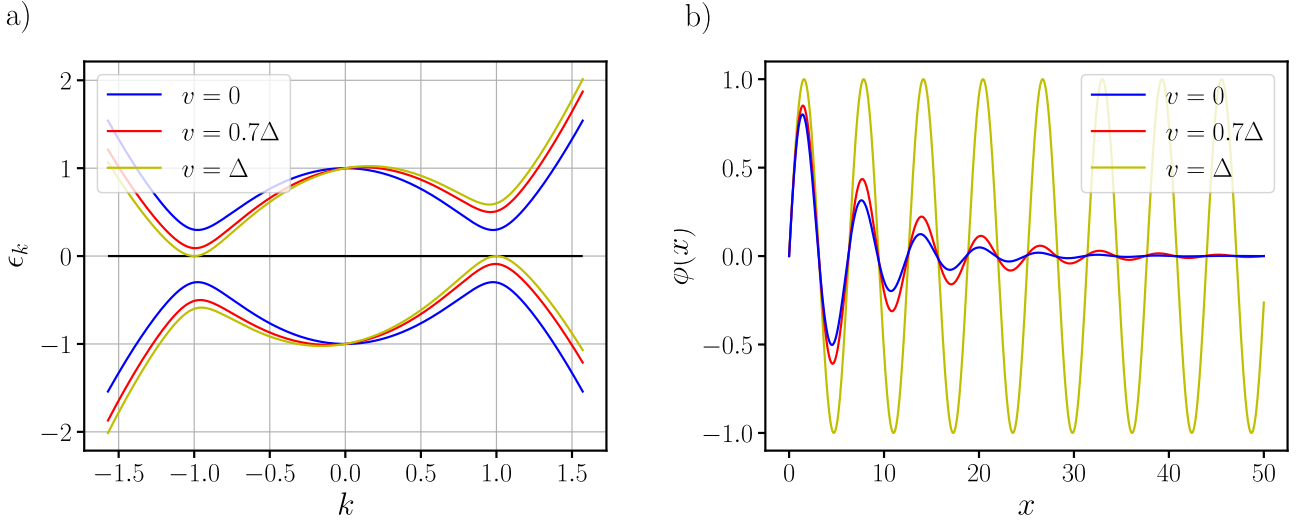


FIG. A1. a) Mode dispersion in the moving frame for several different velocities. b) Localization of the Majorana zero modes in the moving frame for several different velocities. It can be seen that the gap closes for $v = v_{crit} = \Delta$ and simultaneously the Majoranas delocalize in the moving frame.

for the velocity of the left domain wall in Eq. 2. When v_{max} is not extremely large, i.e. the amplitude of the left domain wall position can be considered small compared to the total length of the wire N , we can treat this motion as a time-dependent perturbation and apply perturbation theory. In this case we write the external potential as $V = V_0 + \delta V \sin \omega t$ in which V_0 is the static domain wall profile in Eq. 2 and $\delta V \sin \omega t$ a time-dependent fluctuation on top of it. From Fermi's Golden Rule for a harmonic perturbation [114] we can find the infidelity rate to be

$$\lim_{T \rightarrow \infty} \frac{\mathcal{I}(T)}{T} = \lim_{T \rightarrow \infty} \frac{1}{T} [1 - |\langle \psi_0 | \exp \left\{ -i \int_0^T \mathcal{H}(t) dt \right\} | \psi_0 \rangle|^2] = \lim_{T \rightarrow \infty} \frac{1}{T} \sum_{i \neq 0} |\langle \psi_i | \exp \left\{ -i \int_0^T \mathcal{H}(t) dt \right\} | \psi_0 \rangle|^2 = \quad (\text{A5})$$

$$2\pi \sum_{i \neq 0} (\delta(E_i - E_0 + \omega) + \delta(E_i - E_0 - \omega)) |\langle \psi_i | \delta V | \psi_0 \rangle|^2 \quad (\text{A6})$$

in which $|\psi_i\rangle$ are the eigenstates of the Hamiltonian with the static domain wall profile V_0 which have energy E_i .

From this equation we can read off that there are resonances in the infidelity whenever $\omega_{res} = \pm(E_i - E_0)$, for the first excited state $\omega_{res} = E_i - E_0 = \Delta k_F$ is equal to the gap in the system and we arrive at the resonance time $T_{res} = \frac{2\pi}{\omega_{res}} = \frac{2\pi}{\Delta k_F}$. The resonances for the higher energy bands are suppressed with the transition amplitude $|\langle \psi_i | \delta V | \psi_0 \rangle|^2$. When $\omega \mapsto \infty$ there are no resonances and the infidelity becomes zero; the intuition for this is that the static system H_0 does not notice the harmonic perturbation because it oscillates at a much higher frequency. Similarly, when $\omega < \omega_{res}$ there are also no resonances because the frequencies are smaller than the gap which corresponds to adiabatic Majorana motion.

In the Majorana motion problem in the main text we are however looking at moving the left domain wall forward from x_A to x_B . As shown in Fig. A2 we see that the same resonance time scale emerges for forward motion with

$$v_L(t) = v_{max} \frac{1 - \cos \omega t}{2}. \quad (\text{A7})$$

For $\omega \mapsto \infty$ we get the same rate as constant motion with $\frac{v_{max}}{2}$ which can be explained for low velocities from adiabaticity.

Appendix B: Algorithm and Analysis of the Derivative of the Infidelity

In this appendix we first outline the algorithm we use to compute the many-body overlap Eq. 3 for the Majorana wire setup. Afterwards we argue that all operations in this algorithm are differentiable and we can obtain the derivative of the fidelity with respect to control parameters using automatic differentiation. In the end we show the numerical obtained derivatives and check them with finite difference methods.

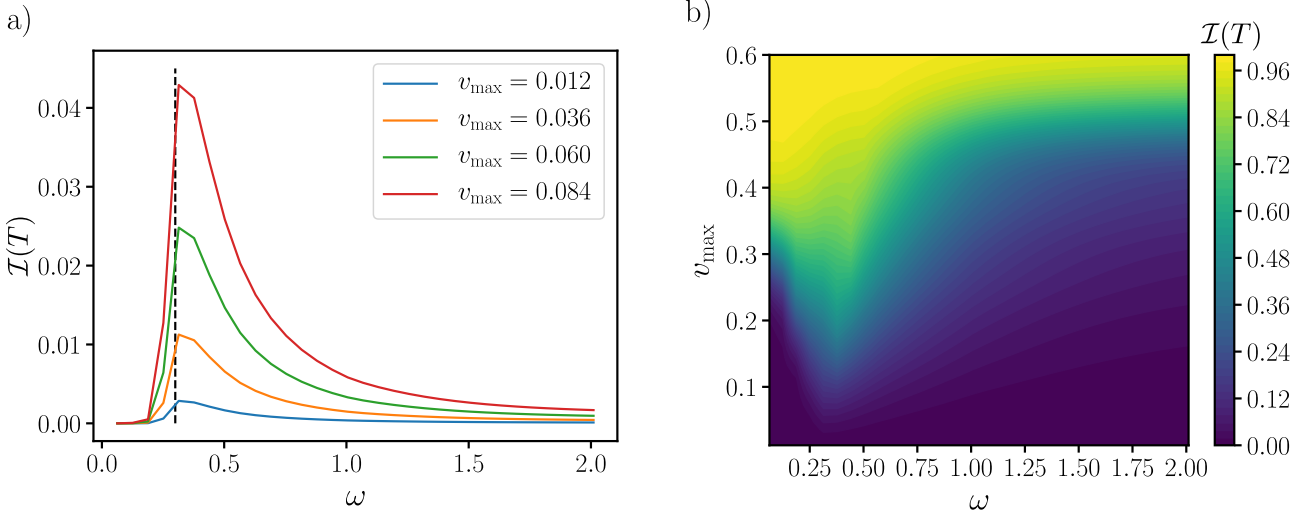


FIG. A2. a) Infidelity as a function of frequency ω , the black dashed line indicates the resonance frequency $\omega_{\text{res}} = \Delta k_F = 0.3$. At $\omega \mapsto \infty$ the infidelity is the same as for constant linear motion with $x_L(t) = \frac{v_{\max}}{2}t$. b) Infidelity as a function of frequency and v_{\max} . For velocities $v_{\max} > v_{\text{crit}} = 0.3$ there are no low adiabatic frequencies anymore. The parameters used in these simulations are $N = 140$, $\mu = 1$, $w = 1$, $\Delta = 0.3$ and $\sigma = 1$.

To find the fidelity we first write the Hamiltonian Eq. 1 in Bogolyubov-de-Gennes (single-particle) form [75, 115]

$$\mathcal{H}(t) = \frac{1}{2}C^\dagger H_{\text{BdG}}(t)C \quad (\text{B1})$$

with $C^\dagger \equiv [c_1^\dagger \dots c_i^\dagger \dots c_N^\dagger \quad c_1 \dots c_i \dots c_N]$ and diagonalize it

$$H_{\text{BdG}}(t)W(t) = E(t)W(t) \quad (\text{B2})$$

in which the columns of $W(t) = \begin{bmatrix} u(t) & v(t)^* \\ v(t) & u(t)^* \end{bmatrix}$ are the eigenmodes (quasi-particle modes) of the BdG Hamiltonian and $E(t)$ is the diagonal matrix of the mode energies $[E]_{ii}(t) = \epsilon_i(t)$. To compute the final many-body overlap at time $t = T$ we then use the Onishi Formula

$$\mathcal{F}(T) = |\langle \psi_B | \psi(T) \rangle|^2 = \det(u_B^* u(T) + v_B^* v(T)) \quad (\text{B3})$$

which relates the BdG quasi-particle picture to the many-body picture. In this $u(T)$ and $v(T)$ can be obtained from $W(T) = \mathcal{T}e^{-i \int_0^T H_{\text{BdG}}(t') dt'} W(0)$ and u_B and v_B from the diagonalization of the instantaneous BdG Hamiltonian with the domain wall at position x_B . $\mathcal{F}(T)$ can now be used to compute the infidelity $\mathcal{I}(T)$ in Eq. 3 in the main text.

From a programming perspective, a code to compute the infidelity from Eq. B3 and Eq. 3 consists of a series of elementary operations (primitives) f_i that map the input control $x_L(t)$ with $t \in [0, T]$ to the output $\mathcal{I}(T) = f_n \circ f_{n-1} \circ \dots \circ f_1(x_L(t))$. The required primitives for this algorithm are matrix multiplications, diagonalization of a hermitian matrix B2 and taking the determinant B3. Each of these operations has a known forward and reverse mode derivative [116] that can be recursively assembled in the chain rule

$$\frac{d\mathcal{I}}{dx_L} = \frac{df_n}{df_{n-1}} \frac{df_{n-1}}{df_{n-2}} \dots \frac{df_1}{dx_L} \quad (\text{B4})$$

to find the derivative of the infidelity with respect to the control.

An automatic differentiation package, like the JAX library [102], computes all the derivatives of the primitives in a code automatically and assembles them in the chain rule to evaluate the total gradient of a computer program. We applied this method to the code to compute the infidelity and used the gradient for the optimizations described in the main text. In Fig. A3 we show an example for the gradient obtained in this way for a linear motion protocol in regime I which we checked with finite difference to make sure it was working correctly. We observe that for this protocol the gradient is the biggest at the boundary which might explain the jumping behaviour at the beginning and end of the protocols we found with the ML optimizations (Fig. 2).

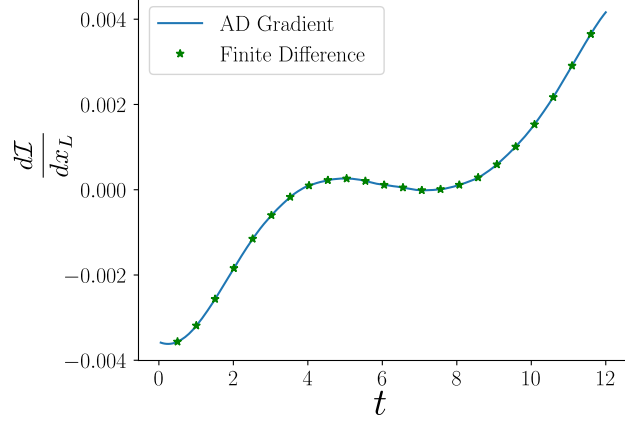


FIG. A3. Comparison between the gradient of the infidelity \mathcal{I} with respect to the control x_L obtained with automatic differentiation (AD) and finite difference. The gradients $\frac{d\mathcal{I}}{dx_L}$ were evaluated for a linear protocol $x_L(t) = v_{\text{avg}}t$ as a function of time t in regime I. The AD gradient matches up with the finite difference gradient and we note that at the beginning and end of the protocol the magnitude of the gradient is the largest.

Appendix C: Gradient Formula for Natural Evolution Strategies

Denote $p_\theta(\phi)$ for the Gaussian distribution $\phi \sim \mathcal{N}(\theta, \sigma^2 I)$ with σ fixed. It follows that [104]

$$\nabla_\theta \mathbb{E}_{\phi \sim \mathcal{N}(\theta, \sigma^2 I)} [\mathcal{I}(T, \phi)] = \nabla_\theta \int p_\theta(\phi) \mathcal{I}(T, \phi) d\phi \quad (\text{C1})$$

$$= \int p_\theta(\phi) \nabla_\theta \log p_\theta(\phi) \mathcal{I}(T, \phi) d\phi \quad (\text{C2})$$

$$= \int p_\theta(\phi) \frac{(\phi - \theta)}{\sigma^2} \mathcal{I}(T, \phi) d\phi. \quad (\text{C3})$$

With change of variable $\phi = \theta + \sigma\epsilon$, we have

$$\nabla_\theta \mathbb{E}_{\phi \sim \mathcal{N}(\theta, \sigma^2 I)} [\mathcal{I}(T, \phi)] = \int p_\epsilon(\epsilon) \mathcal{I}(T, \theta + \sigma\epsilon) \epsilon / \sigma d\epsilon \quad (\text{C4})$$

$$= \mathbb{E}_{\epsilon \sim \mathcal{N}(0, I)} [\mathcal{I}(T, \theta + \sigma\epsilon) \epsilon / \sigma]. \quad (\text{C5})$$

Appendix D: Comparing standard benchmark protocols and different parameterizations of the control

In addition to the SA benchmark results of $N = 110$ in the main paper, we have also performed optimizations on a smaller system size $N = 50$ with various representations and compared them to standard bang-bang [70, 90] and super-adiabatic ramp-up-down protocols [71].

For a standard bang-bang protocol the velocity of the domain wall v_L is at all times only allowed to take either the value $v_L = v_{\text{min}}$ or the value $v_L = v_{\text{max}}$, a switch between these two discrete velocities is called a bang. To keep the number of free parameters manageable we tested periodic protocols in which the time between consecutive bangs is held constant. Moreover, we used $v_{\text{min}} = 0$ and $0 < v_{\text{max}} < v_{\text{crit}}$ similar to the protocols in [70].

The ramp-up-down protocols are a family of super-adiabatic protocols in which the velocity is slowly built up from zero to some maximum velocity v_{max} and then ramped down again to zero as given by

$$v_L(t) = \begin{cases} v_{\text{max}} \frac{1 - \cos \omega t}{2}, & 0 \leq t \leq \frac{\pi}{\omega} \\ v_{\text{max}}, & \frac{\pi}{\omega} \leq t \leq \frac{\pi}{\omega} + T \\ v_{\text{max}} \frac{1 - \cos(\omega t - \omega T)}{2}, & \frac{\pi}{\omega} + T \leq t \leq \frac{2\pi}{\omega} + T \\ 0, & \text{otherwise} \end{cases} \quad (\text{D1})$$

in which ω is the parameter that determines how quickly the velocity is accelerated to v_{\max} .

In Table A1 we summarize the best results (lowest infidelity) of these protocols obtained from scanning over the free parameters. We compared these results to protocols obtained with the ML methods as described in the main text and see that in all regimes the ML protocols outperform the standard benchmark protocols significantly.

| Regime | linear | bang-bang | ramp-up-down | SA | DP | NES |
|--------|----------|-----------|--------------|----------|----------|----------|
| I | 0.477283 | 0.437695 | 0.493434 | 0.396896 | 0.415888 | 0.394496 |
| II | 0.192793 | 0.169737 | 0.203298 | 0.147863 | 0.153108 | 0.145300 |
| III | 0.012011 | 0.008888 | 0.0131240 | 0.006467 | 0.007034 | 0.006904 |
| IV | 0.006887 | 0.006752 | 0.004607 | 0.000078 | 0.000143 | 0.000379 |

TABLE A1. Results for the infidelity $\mathcal{I}(T)$ of different benchmark protocols (first three columns) in regime I-IV compared to results obtained with SA, AD and NES. For these simulations (l, T) are $\{(4.32, 12), (3.15, 14), (0.48, 8), (2.4, 40)\}$, $N = 50$ and the other parameters of the Majorana wire setup are the same as for figure 2 in the main text.

We also tested the NES and DP optimization algorithms for different parameterizations of the control of the domain wall before fixing the specific parameterizations as used and described in the main text. We compared parameterizing the control by the position $x_L(t)$, the velocity $v_L(t)$ or a neural network $x_L(t) = \text{NN}_\theta(t)$ and show the results in Table A2. The optimization with NES gives the lowest infidelity when we parameterize by position in regimes I and II and by velocity in regimes III and IV. For the DP optimization the best infidelity optimizes a neural network in regimes I,III and IV and optimizes over the position in regime II.

| Regime | DP neural net | DP position | NES position | NES velocity | NES neural net |
|--------|---------------|-------------|--------------|--------------|----------------|
| I | 0.390974 | 0.415888 | 0.394496 | 0.400802 | 0.458588 |
| II | 0.154106 | 0.153108 | 0.145300 | 0.150894 | 0.184216 |
| III | 0.006400 | 0.007034 | 0.012008 | 0.006904 | 0.008375 |
| IV | 0.000143 | 0.002368 | 0.014757 | 0.000379 | 0.000690 |

TABLE A2. Comparison of the lowest infidelity values between optimizations of AD and NES with respect to different parameterizations of the control (position $x_L(t)$, velocity $v_L(t)$ and neural net $x_L(t) = \text{NN}_\theta(t)$). Based on these testing values we determined which parameterizations to use for the optimizations in the main text.

Appendix E: Parameters and interpolation of the optimized JMJ model strategy

In this appendix we give the parameters of the optimized JMJ strategies in regimes I,II, and III as shown in Fig. 1 d) in the main text and verify how close these strategies are to the protocols obtained with the ML methods.

In the main text we observed that dressed JMJ protocols with the lowest infidelities have a linear relation between $\Delta x_{\text{forward}}$ and $\Delta x_{\text{backward}}$ as Fig. 3 shows. To attain the best JMJ protocols in regime I-III, we scan through $\Delta x_{\text{forward}}$ and Δx_{back} with respect to the linear relation in each regime and pick the one which gives the overall lowest infidelity. The parameters of the resulting JMJ strategies are provided in Table A3 and the strategies are shown in Fig. 1.

| Regime | $\Delta x_{\text{forward}}$ | Δx_{back1} | Δt_{back} | Infidelity |
|--------|-----------------------------|---------------------------|--------------------------|------------|
| I | 7.992 | 7.5099789 | 0.05 | 0.35747148 |
| II | 1.90928571 | 1.54962755 | 0.31 | 0.15885453 |
| III | 0.548210 | 0.457123 | 0.33 | 0.0056574 |

TABLE A3. Best dressed JMJ model strategies parameters and their corresponding infidelities obtained from scans over $\Delta x_{\text{forward}}$, Δx_{back} and Δt_{back} . The corresponding profiles are shown in Fig. 1 in the main paper.

We linearly interpolate these best JMJ model strategies to the machine learning protocols in the main paper (Fig. 2) to see whether there are additional protocols that are better in terms of infidelity. The results for this in regime III with the DP strategy are shown in Fig. A4 from which we can see that the DP strategy is slightly better than the JMJ (due to more free parameters) and that there are no other local minima in between them. For the other regimes and interpolations from the NES strategy we obtained similar results, or only small improvement in the interpolation.

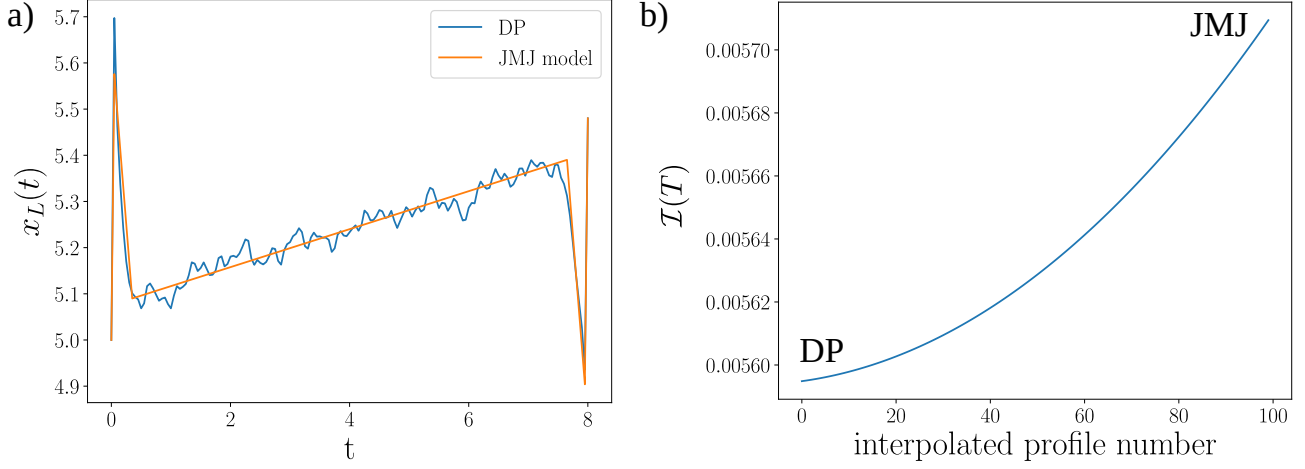


FIG. A4. a) The DP optimized majorana motion strategy in regime III ($T = 8, l = 0.48$) on top of the optimized (scans over the free parameters) JMJ model strategy. The optimal JMJ model strategy captures the main features (jumps) of the DP strategy well. b) Infidelity $\mathcal{I}(T)$ obtained for 100 linearly interpolated profiles between the DP strategy and JMJ model strategy as shown in panel a). We observe a convex decreasing function towards the more flexible DP result.